Cell Reports

Article

The Amot/integrin protein complex transmits mechanical forces required for vascular expansion

Graphical abstract

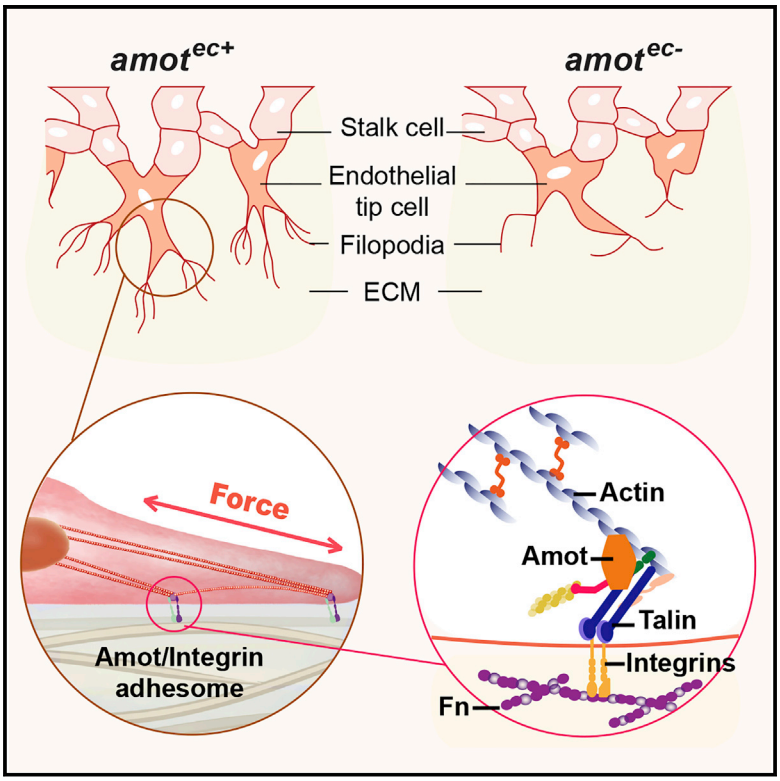

Highlights

- Angiomotin is required for vascular expansion
- Angiomotin is an important component of the integrin adhesome
- Angiomotin relays mechanical signals from the integrins to the cytoskeleton

Authors

Yuanyuan Zhang, Yumeng Zhang, Sumako Kameishi, ..., Thomas H. Barker, Federica Cavallo, Lars Holmgren

Correspondence

lars.holmgren@ki.se

In brief

Zhang et al. demonstrate that the scaffold protein Angiomotin binds to the integrin complex by Talin and thus relays mechanical forces between the extracellular matrix and cytoskeleton. This exchange of mechanical forces is essential for endothelial migration during postnatal retinal vascular expansion, as well as during tumor angiogenesis.

Zhang et al., 2021, Cell Reports *36*, 109616
August 24, 2021
https://doi.org/10.1016/j.celrep.2021.109616

CellPress

Cell Reports

CellPress
OPEN ACCESS

Article

The Amot/integrin protein complex transmits mechanical forces required for vascular expansion

Yuanyuan Zhang,[1] Yumeng Zhang,[1] Sumako Kameishi,[1] Giuseppina Barutello,[2] Yujuan Zheng,[1] Nicholas P. Tobin,[1] John Nicosia,[3] Katharina Hennig,[5] David Kung-Chun Chiu,[1] Martial Balland,[5] Thomas H. Barker,[4] Federica Cavallo,[2] and Lars Holmgren[1,6,*]

[1]Department of Oncology-Pathology, Bioclinicum, Karolinska Institutet, Stockholm 17164, Sweden
[2]Department of Molecular Biotechnology and Health Sciences, Molecular Biotechnology Center, University of Turin, Turin 10126, Italy
[3]Wallace H. Coulter Department of Biomedical Engineering, Georgia Institute of Technology, Atlanta, GA 30332, USA
[4]Department of Biomedical Engineering, University of Virginia, Charlottesville, VA 22904, USA
[5]Laboratoire Interdisciplinaire de Physique, Université Joseph Fourier (Grenoble 1), Saint Martin d'Hères Cedex, 38402, France
[6]Lead contact
*Correspondence: lars.holmgren@ki.se
https://doi.org/10.1016/j.celrep.2021.109616

SUMMARY

Vascular development is a complex multistep process involving the coordination of cellular functions such as migration, proliferation, and differentiation. How mechanical forces generated by cells and transmission of these physical forces control vascular development is poorly understood. Using an endothelial-specific genetic model in mice, we show that deletion of the scaffold protein Angiomotin (Amot) inhibits migration and expansion of the physiological and pathological vascular network. We further show that Amot is required for tip cell migration and the extension of cellular filopodia. Exploiting *in vivo* and *in vitro* molecular approaches, we show that Amot binds Talin and is essential for relaying forces between fibronectin and the cytoskeleton. Finally, we provide evidence that Amot is an important component of the endothelial integrin adhesome and propose that Amot integrates spatial cues from the extracellular matrix to form a functional vascular network.

INTRODUCTION

Most, if not all, organs are dependent on the formation of an organized blood circulatory network to function properly. The mechanisms that control the ingrowth of vessels have garnered much attention given its importance in the pathogenesis of various disease conditions such as ischemia, cancer, and diabetes (Folkman, 1995; Potente et al., 2011). The *de novo* blood vessel formation, namely, angiogenesis, is triggered by morphogenic gradients that promote orderly collective migration of endothelial cells (ECs) that give rise to a blood circulatory network (Gerhardt and Betsholtz, 2005; Eilken and Adams, 2010). Endothelial tip cells guide the expanding vessel network and probe the environment by extending cellular protrusions, known as filopodia (Gerhardt et al., 2003). These filopodia not only detect and respond to chemotactic factors such as VEGF-A and axon guidance factors but also mechanically interact with the surrounding extracellular matrix (ECM). The ECM exerts mechanical control on the endothelium by binding to integrins that relay forces to the cellular cytoskeleton (Hynes, 2002; Schwartz, 2010). Here, integrins form a tension-dependent link between fibrillar ECM and the cytoskeleton that is critical for translating mechanical forces into biochemical signals (Geiger et al., 2001). The actual tension is generated by actomyosin contraction, which provides the tractional force required for migration together with the actual stiffness of the ECM (Zhang et al., 1997; Zhong et al., 1998; Baneyx et al., 2002). A major component of the developing blood vessels is Fibronectin (Fn) (Pankov and Yamada, 2002). The Fn-binding endothelial integrins $\alpha5\beta1$ and $\alpha v\beta3/\beta5$ integrin receptors have emerged as possible targets for anti-angiogenic therapies. However, the mechanisms of these molecular pathways in controlling angiogenesis are complex. Inactivation of integrin $\alpha5$ and αv during mouse development causes death *in utero* due to vascular defects (Murphy et al., 2015). Although highly expressed in tumor endothelium, conditional deletion of Fn, $\alpha5\beta1$, and $\alpha v\beta3/\beta5$ does not inhibit tumor expansion, which suggests the upregulation of alternative compensatory pathways. Indeed, analysis of the integrin adhesome has identified over 180 proteins, with some of them regulated by actin tension (Zaidel-Bar and Geiger, 2010, Schiller et al., 2011). Further insight on how mechanical forces are transduced may provide perspective on how these pathways could be targeted in a more efficient way.

In this report, we have studied the role of Angiomotin (Amot) in the transmission of force during EC migration. We have previously reported the identification of the Amot protein family, which consists of three members, namely, Amot, Amot-Like 1 (AmotL1), and AmotL2 (Bratt et al., 2002). All three members are scaffold proteins characterized by a coiled-coil and WW domains, as well as a post synaptic density protein (PSD95), Drosophila disc large tumor suppressor (Dlg1), and zonula occludens-1 protein (zo-1) (abbreviated PDZ)-binding motif, and each of them has two

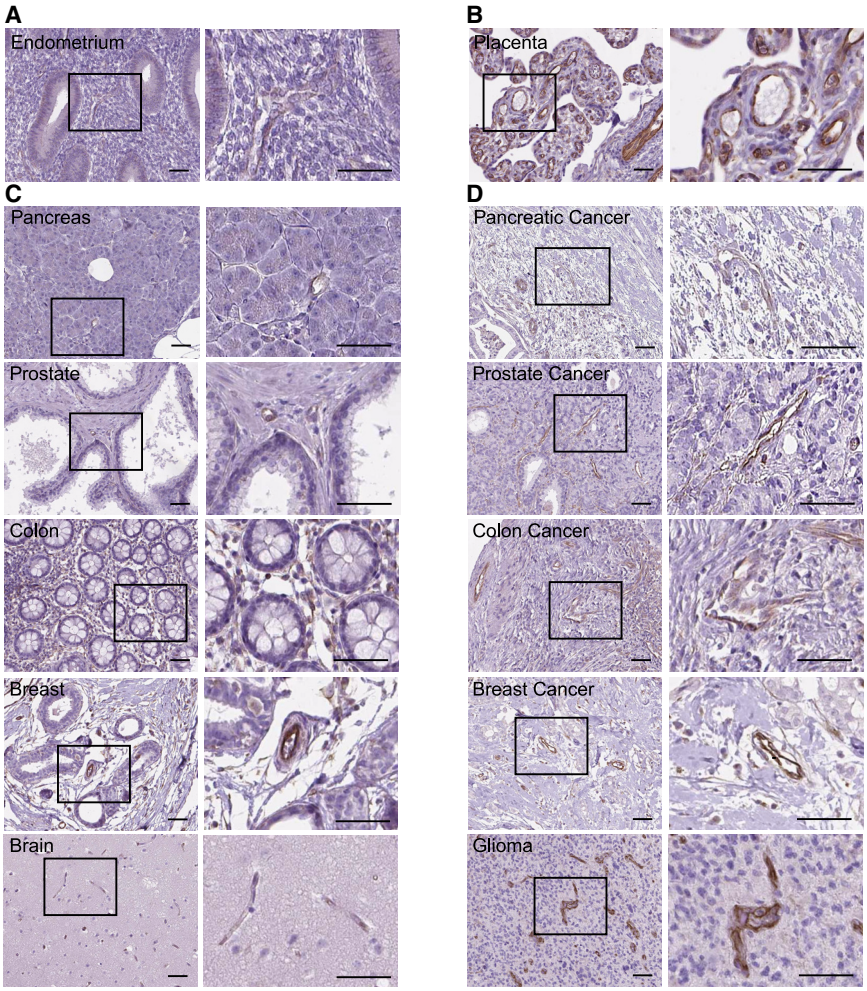

Figure 1. Localization of Amot in blood vessels of human tissues

(A–D) Immunohistochemical (IHC) localization of Amot protein. Rabbit Amot antibodies were generated against the C-terminal 20 amin acids (aa) and immunoaffinity purified. The IHC of patient samples was performed in collaboration with Human Protein Atlas (Uhlén et al., 2015). Detailed information of patient samples is listed in the Key resources table. Human paraffin sections of endometrium (A) and placenta (B) were stained with Amot antibodies, with a positive signal shown in brown. (C and D) Representative images of Amot protein expression in normal tissues, including in pancreas, prostate, colon, breast, and brain, as well as in corresponding cancerous tissues. Right panels show magnification of boxed areas. Scale bars, 50 μm. See also Figure S1.

identified isoforms, including p130/p80 Amot, p100/p90 AmotL1, and p100/p60 AmotL2. They are of interest as they bind and localize membrane receptors with polarity proteins complexes and regulate the Hippo pathway and the cytoskeleton. We have recently shown that Amot, AmotL1, and AmotL2 exert distinct functions in blood vessel development by using zebrafish and conditional knockout mice (Zheng et al., 2016; Hultin et al., 2014). AmotL2 was demonstrated to bind to the VE-cadherin complex and is required for formation of radial actin filaments. These filaments transduce force at the cellular junctions, and inactivation in mouse and zebrafish embryos abrogates aortic expansion. A similar function of AmotL2 is found in epithelial cells where AmotL2 binds to E-cadherin, organizes radial actin filaments, and is required for blastocyst hatching in pre-implantation embryos (Hildebrand et al., 2017). Amot was the original protein of this family and is essential for EC migration. In this study, we investigated the role of Amot in angiogenesis, setting up its involvement in the transmission of force in ECs. We used an endothelial-specific mouse knockout model to study postnatal angiogenesis. We present evidence that Amot is a part of the endothelial integrin adhesome and is essential for force transmission between ECM, integrins, and the actin cytoskeleton.

RESULTS

Amot is expressed in blood vessels of human placenta, as well as human tumors

We have previously reported a preferential expression of Amot in ECs during physiological angiogenesis of zebrafish and mouse (Aase et al., 2007). In addition, recent publications have implicated Amot as a regulator of the Hippo pathway in epithelial cells *in vitro*, suggesting a role in carcinogenesis (Zeng et al., 2017). To clarify this apparent discrepancy, we analyzed the Amot expression pattern in normal and cancerous human tissues. The Amot expression pattern was mapped in both normal and pathological tissue sections with immunoaffinity-purified Amot antibodies, which do not cross-react with AmotL1 or AmotL2 (Levchenko et al., 2003). Amot positivity was restricted to blood vessels of third-trimester placenta but was not detectable in adult endometrium (Figures 1A and 1B). Furthermore, protein expression was not detectable in areas outside blood vessels in adult tissues such as pancreas, brain, breast, prostate, and colon (Figure 1C). In addition to blood vessels of angiogenic tissues, Amot staining was also detected in blood vessels of the adult epididymis and in podocytes of the kidney glomeruli (Figures S1A and S1B). Analysis of human cancers of different origins showed an apparent upregulation of Amot in tumor blood vessels and stroma, whereas the adjacent tumor cells were negative (Figure 1D; Figures S1C–S1F).

Amot is essential for endothelial tip cell migration

The mouse retina is an established model for the study of physiological angiogenesis, as it becomes vascularized in a highly reproducible manner over the first 10 days after birth (Pitulescu et al., 2010; Uemura et al., 2006). We performed whole-mount immunofluorescence (IF) staining to detect Amot expression at neonatal (day 6) and in adult retinas. Amot was ubiquitously expressed in

retinal vessels at postnatal day 6 (P6), whereas little signal above background was detected in retinas of 4-week-old mice (Figure 2A). We further analyzed Amot steady-state protein levels in whole retinas at postnatal day 6 (P6) as well as retinas from adult mice. The results showed that Amot expression decreased by 60% from P6 compared with the adult stage (Figures 2B and 2C).

Our previous studies showed that 75% of Amot conventional knockout mice die before embryonic day 12 due to severe vascular defects (Aase et al., 2007). To study the role of Amot in normal and tumor angiogenesis in postnatal mice, we used an inducible genetic deletion approach to silence Amot expression in ECs. To inactivate Amot (localized on the X chromosome) in a cell-type-specific fashion, we crossed mice containing loxP sites flanking exon 4 and 5 with Cdh5 (PAC)^{CreERT2} transgenic mice (hereafter abbreviated *amot*$^{ec+}$ or *amot*$^{ec-}$) (Pitulescu et al., 2010). This model allowed efficient tamoxifen-inducible recombinase expression in ECs. Tamoxifen-induced recombination at P6 was verified by genomic PCR analysis and monitored at a cellular level by the activation of the ROSA26-EYFP reporter (Figure S2A).

To investigate the role of Amot during postnatal retinal angiogenesis, we induced Cre recombinase activity by injecting tamoxifen at P1–P3. The retinas were harvested at P6, dissected, and analyzed by whole-mount staining. Inactivation of *amot* resulted in inhibition of radial vessel expansion, which appeared non-symmetrical and partially collapsed (Figures 2D and 2E). Endothelial tip cells guide vessel expansion and sense environmental cues by the extension of filopodia. Quantification of tip cells showed a significant decrease in the number of tip cells per a certain length of vascular outline in *amot*$^{ec-}$ retinas, compared with *amot*$^{ec+}$ retinas (Figures 2F and 2G). In addition, *amot*$^{ec-}$ tip cells exhibited a 4-fold reduction in the number of filopodial extensions (Figures 2H and 2I). In contrast, deletion of *amot* in adult mice did not result in detectable aberrations of the retinal vasculature (Figure S2B).

Amot is required for endothelial tip cell positioning

Our data show that Amot is expressed in both tip cells and capillaries of developing retinas. However, Amot depletion seemed to primarily affect EC tip cells. To further investigate this apparent discrepancy, we made use of the fact that injection of decreasing doses of tamoxifen results in lower recombination frequencies. To trace and follow the positioning of individual ECs, we crossed *amot*$^{ec+}$ mice with ROSA26-EYFP Cre-reporter mice (Srinivas et al., 2001). Cre activity was monitored by estimating the ratio of YFP positivity in EC cells in tip cell position versus the overall recombination in the capillary bed (Figures 3A and S3A). In *amot*$^{ec+}$/ROSA26-EYFP retinas, the frequency of YFP$^+$ tip cells plotted against YFP$^+$ capillary ECs showed a strong linear relationship and therefore no difference in recombination at the two distinct sites (Figure 3B). We then compared the recombination frequency of *amot*$^{ec+}$ and *amot*$^{ec-}$ tip cells (Figures 3C and S3B–S3D). At a 50%–85% recombination rate, the ratio of YFP$^+$ tip cells to capillaries in *amot*$^{ec+}$ ECs was approximately 1. In contrast, the corresponding ratio of *amot*$^{ec-}$ retinas was significantly lower (0.3), indicating a decreased ability of Amot-depleted ECs to occupy tip cell position (Figure 3C). Higher recombination frequencies (85%–100%) forced *amot*$^{ec-}$ tip cells to localize at the leading edge with severe phenotypic defects (Figures 3D and 3E).

Amot relays mechanical force between matrix and ECs

To generate functional vessels, ECs are dependent on the active interaction with other cell types, including pericytes, microglia, and astrocytes (Fruttiger, 2007). The latter migrate a few days earlier than ECs and act as a guiding template for the patterning of the vascular network in the retina (Fruttiger et al., 1996; Jiang et al., 1994). We used the astrocyte marker Glial Fibrillary Acidic Protein (GFAP) to investigate whether *amot* depletion in ECs affected astrocyte patterning in a non-autonomous manner. In *amot*$^{ec+}$ retinas, GFAP staining was oriented in a radial pattern around tip cells in the vascular/astrocyte border zone, suggesting that tip cells remodeled the astrocyte network by exerting mechanical force (Figure 4A). Interestingly, the apparent radial deformations of the astrocytes around tip cells were not observed in *amot*$^{ec-}$ retinas (Figure 4A). These observations prompted us to investigate whether Amot is required for the interaction between the migrating tip cells and the pre-existing astrocytes.

As previously mentioned, astrocytes migrate into the retina, prior to the onset of angiogenesis, and deposit a network of ECM that acts as guidance cue to migrating ECs (Turner et al., 2017). A major component of this ECM is Fn, which forms fibrils that display elasticity when subjected to mechanical force (Klotzsch et al., 2009). Indeed, *in vitro* evidence indicates that Fn molecules are exposed to cell-derived forces and in response exhibit molecular strain (Lemmon et al., 2009). To further investigate the interaction of EC tip cells and astrocytes, we first mapped the Fn expression in P6 retinas. IF staining showed the intense expression of Fn in astrocytes ahead of the vascular front and around tip cells as previously reported (Stenzel et al., 2011), whereas Fn was not detectable in the basal membrane of mature vessels of adult mice (Figure S4A). An analysis of Fn expression in postnatal *amot*$^{ec-}$ retinas did not reveal any significant differences in expression levels (Figure S4B).

Next, we used enhanced-resolution microscopy to visualize Fn fibrils in areas of interaction between endothelial tip cells and astrocytes. Fn fibrils were stretched and aligned with tip cell filopodia in *amot*$^{ec+}$, whereas Fn was localized to punctate and shorter fibrils in *amot*$^{ec-}$ (Figure 4B; quantification in Figure S4C). Several reports have shown that cell-mediated Fn fibril assembly is regulated by mechano-signals and that cell-generated tractional forces may stretch Fn fibers several-fold (Zhong et al., 1998; Leiss et al., 2008; Dallas et al., 2005). To determine force patterns *in vivo*, we made use of a single-chain antibody (clone H5), generated by Barker and co-workers, that specifically binds the force-extended conformation of the FnIII9-10 integrin-binding domain (Cao et al., 2017). This allows the detection of cryptic epitopes that are masked in a relaxed state but exposed upon mechanical tension. As we have previously published, this method can be used to measure strained Fn in postnatal retinas as well as in pathological conditions such as lung fibrosis (Cao et al., 2017).

A heatmap was generated using the ratio between the signal from the H5 stretch-specific antibody and a pan-Fn antibody detecting both stretched and relaxed forms. An increased ratio of H5 staining was observed in areas where the tip cell filopodia made contact with Fn fibrils in *amot*$^{ec+}$ retinas, suggesting EC-mediated force generation (Figure S4D). We then assessed whether inactivation of *amot* would affect the strained conformation of Fn fibrils

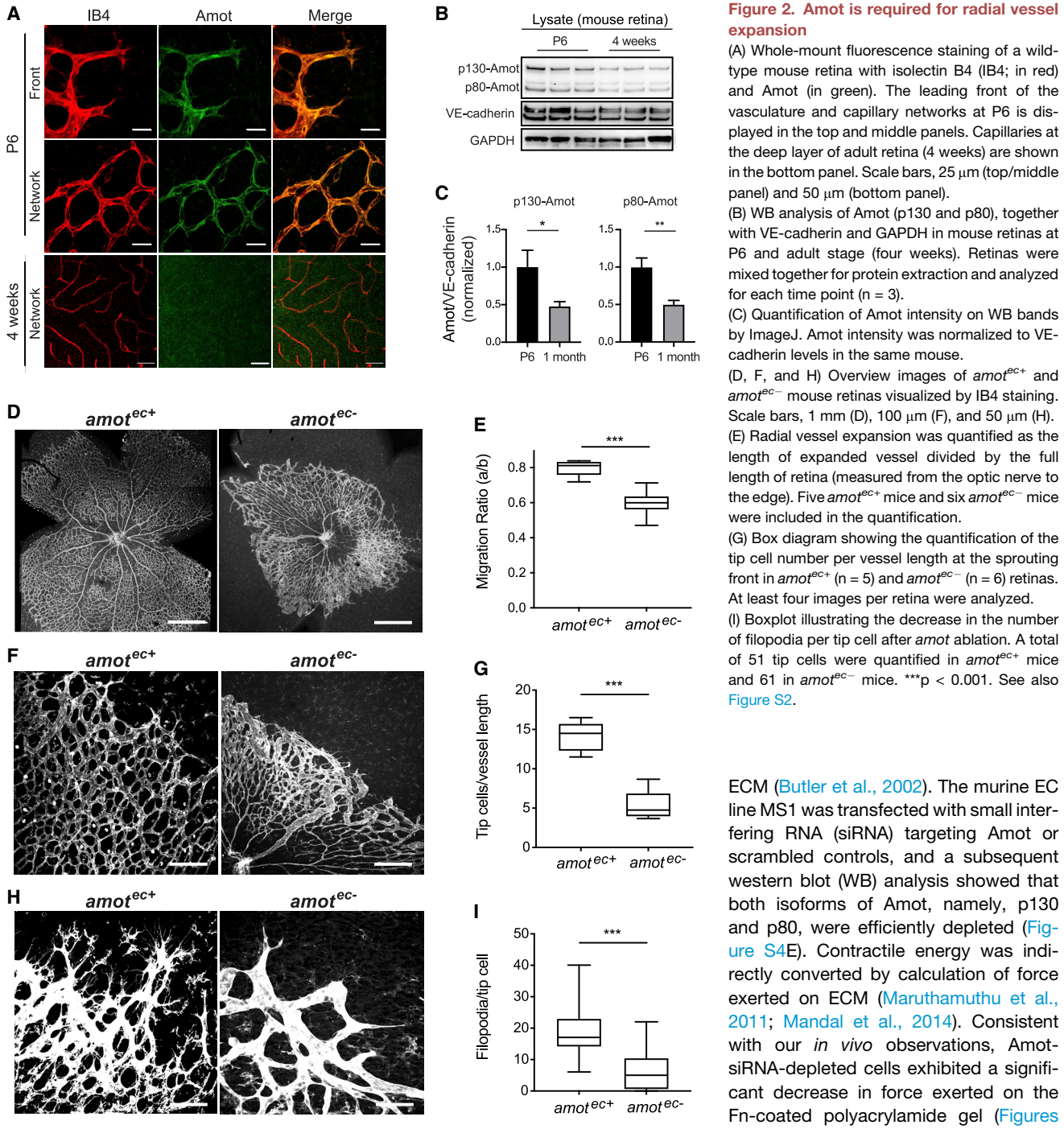

Figure 2. Amot is required for radial vessel expansion

(A) Whole-mount fluorescence staining of a wild-type mouse retina with isolectin B4 (IB4; in red) and Amot (in green). The leading front of the vasculature and capillary networks at P6 is displayed in the top and middle panels. Capillaries at the deep layer of adult retina (4 weeks) are shown in the bottom panel. Scale bars, 25 μm (top/middle panel) and 50 μm (bottom panel).

(B) WB analysis of Amot (p130 and p80), together with VE-cadherin and GAPDH in mouse retinas at P6 and adult stage (four weeks). Retinas were mixed together for protein extraction and analyzed for each time point (n = 3).

(C) Quantification of Amot intensity on WB bands by ImageJ. Amot intensity was normalized to VE-cadherin levels in the same mouse.

(D, F, and H) Overview images of *amot*$^{ec+}$ and *amot*$^{ec-}$ mouse retinas visualized by IB4 staining. Scale bars, 1 mm (D), 100 μm (F), and 50 μm (H).

(E) Radial vessel expansion was quantified as the length of expanded vessel divided by the full length of retina (measured from the optic nerve to the edge). Five *amot*$^{ec+}$ mice and six *amot*$^{ec-}$ mice were included in the quantification.

(G) Box diagram showing the quantification of the tip cell number per vessel length at the sprouting front in *amot*$^{ec+}$ (n = 5) and *amot*$^{ec-}$ (n = 6) retinas. At least four images per retina were analyzed.

(I) Boxplot illustrating the decrease in the number of filopodia per tip cell after *amot* ablation. A total of 51 tip cells were quantified in *amot*$^{ec+}$ mice and 61 in *amot*$^{ec-}$ mice. ***p < 0.001. See also Figure S2.

in the tip cell area. As shown in Figure 4C, non-recombined ECs (YFP^{-}) exhibited a H5/pan-Fn signal ratio similar to that of *amot*$^{ec+}$ retinas. In contrast, YFP^{+} EC showed a marked reduction in the ratio of H5/pan-Fn signal.

We then used traction force microscopy (TFM) to more precisely measure the force involved in the interaction between ECs and the ECM *in vitro*. This method measures cell-generated traction forces by quantifying the deformation of the surrounding ECM (Butler et al., 2002). The murine EC line MS1 was transfected with small interfering RNA (siRNA) targeting Amot or scrambled controls, and a subsequent western blot (WB) analysis showed that both isoforms of Amot, namely, p130 and p80, were efficiently depleted (Figure S4E). Contractile energy was indirectly converted by calculation of force exerted on ECM (Maruthamuthu et al., 2011; Mandal et al., 2014). Consistent with our *in vivo* observations, Amot-siRNA-depleted cells exhibited a significant decrease in force exerted on the Fn-coated polyacrylamide gel (Figures 4D and 4E). Additionally, we observed that depletion of Amot resulted in changes in cell shape and did not elongate upon attachment to the ECM (Figure 4F; Figures S4F and and S4G).

Amot is part of the integrin adhesome

We have previously shown that the other members of the Amot protein family link membrane receptors to the cytoskeleton. Thus, we hypothesized that Amot would function in a similar manner by mediating force from the ECM to the cytoskeleton

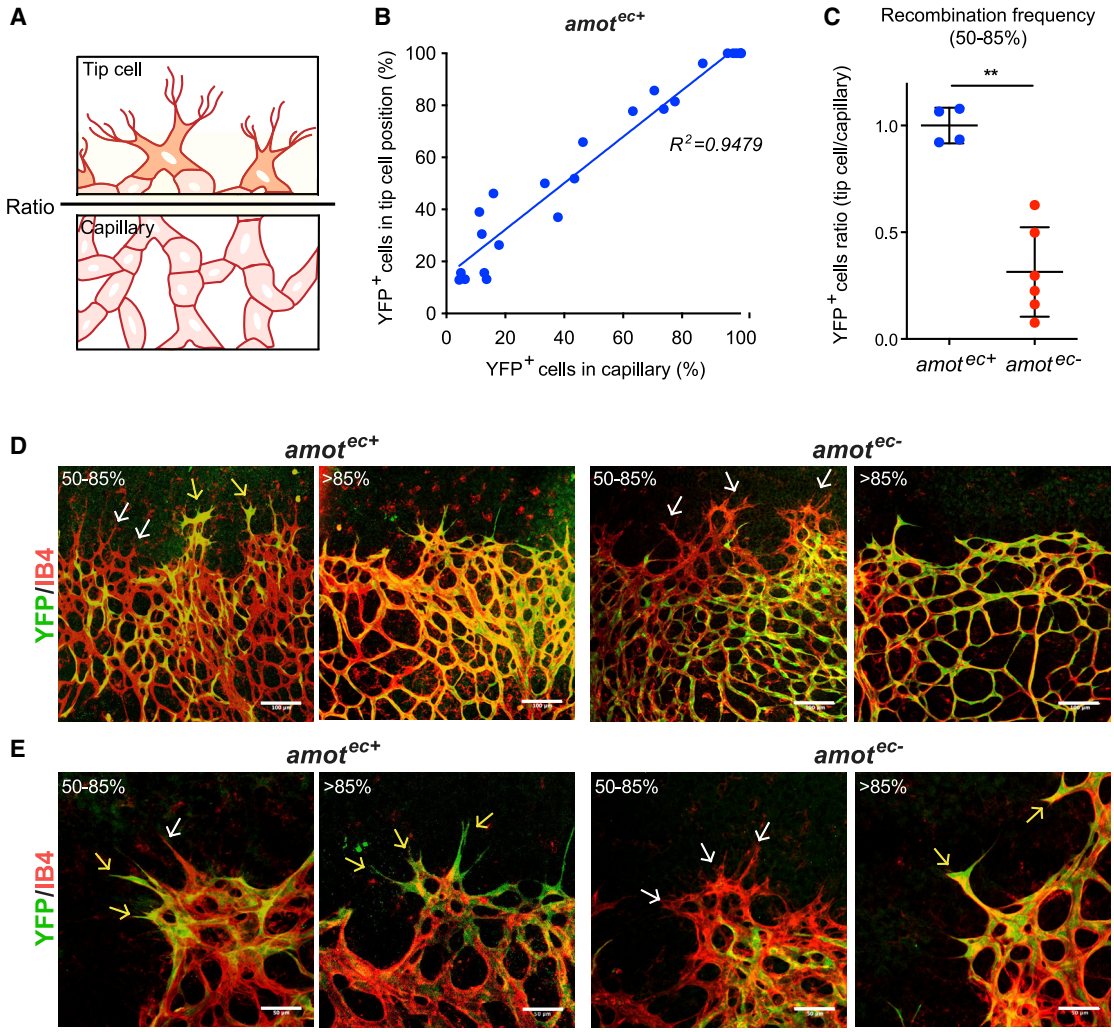

Figure 3. Amot is required for endothelial tip cell positioning

(A) Schematic indicating tip cell and capillary areas of P6 retina, where quantification of recombination was performed. The ratio represents the ROSA26-EYFP-positive (YFP$^+$) cell percentage of the tip cell area divided by that of the overall recombination frequency that was measured in the capillary network.

(B) Linear scatterplot showing a correlation of the recombination (YFP$^+$) ratio between tip cell position and capillary area in *amot*$^{ec+}$ retinas (n = 24). The graph shows a direct linear relationship between the overall (capillary) recombination frequency to that of EC in tip cell position. This means that there is no disadvantage for YFP$^+$, *amot*$^{ec+}$ EC to acquire a tip cell position. The data were analyzed using Pearson's correlation R^2 (*R*-squared) = 0.9479.

(C) The ratio of recombined EC percent at tip cell positions (*tip cell amot*$^{ec+}$, *YFP*$^+$/*Capillary amot*$^{ec+}$, *YFP*$^+$, n = 4) in *amot*$^{ec+}$ retinas was approximately 1 and compared with that of *amot*$^{e-}$ (n = 6) retinas.

(D and E) Distribution of YFP$^+$ cells in *amot*$^{ec+}$ and *amot*$^{ec-}$ retinas at P6 stained for ECs (IB4 in red and YFP in green) at >85% or 50%–85% recombination frequencies as indicated in the figures. Yellow arrows indicate YFP$^+$ tip cells, and white arrows indicate YFP$^-$ cells. **p < 0.01. Scale bars, 100 μm (D) and 50 μm (E). See also Figure S3.

by ECM-binding membrane proteins. In support of this notion, we found that GFP-tagged Amot co-localized with Vinculin in spreading ECs (Figure 5A). To identify potential interacting partners, we performed mass spectrometry (MS) of proteins that were co-immunoprecipitated with Amot in lysates of primary bovine aortic endothelial (BAE) cells. All proteins (299) from the list (Table S1) were selected for pathway analysis by using the Panther 2016 software as described in the STAR Methods. The identified pathways are shown in Figure 5B with the "integrin signaling pathway" and "cytoskeletal regulation by Rho GTPase" appearing as the top regulated pathways (Table S2). In support, several integrin subtypes were also present in the MS data, including β3, α5, and β1 (Figure 5C).

To identify proteins in close proximity of Amot (the Amot adhesome), we used the BioID (proximity-dependent biotin identification) methodology. This method is based on fusing the promiscuous biotin ligase BirA with the protein of interest. When expressed in cells, it can be induced to biotinylate interacting proteins (Roux et al., 2018). We fused the BirA to the N terminus of the p130 and p80 Amot isoforms (schematic shown in Figure 5D). The

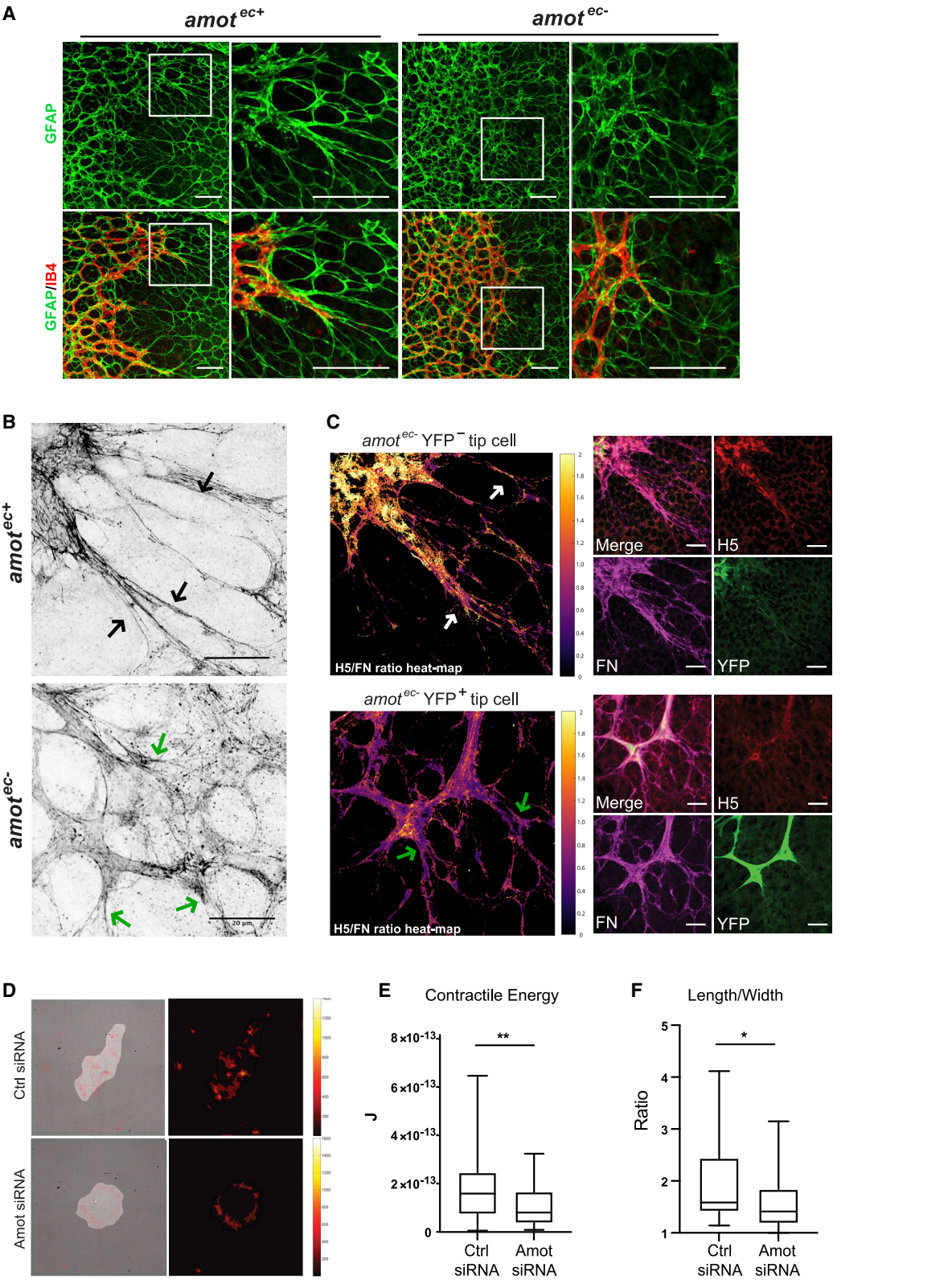

(legend on next page)

constructs were transfected into MS1 ECs and verified using antibodies against the biotinylase and Amot (Figure S5A). BirA tagged to p130-Amot was localized to the cell periphery in sub-confluent cells, which was distinct from those cells expressing the p80-Amot BirA localizing to intra-cellular vesicles (Figure S5B). The BirA-tagged biotinylated proteins were successfully pulled down using streptavidin beads as analyzed by WB (Figure S5C). To identify the interactors of p130- and p80-Amot, MS was performed on streptavidin affinity-purified proteins. A total of 178 proteins with a fold change (fc) of >0 were scored as positive hits (Table S3). A Panther pathway analysis of the positive hits highlighted integrin signaling pathway as the top enriched pathway (Figure 5E; Table S4). Additionally, from the analysis, we also found Zyxin, Kank2, Catenin delta-1, and Myosin 9/10, which have been previously identified as focal-adhesion-related proteins (Figure 5F; Smith et al., 2010; Sun et al., 2016; Rahikainen et al., 2019; Bondzie et al., 2016). The BioID approach also recognized the known direct interactors of Amot such as, Pard3, Nf2, and Yap as shown in Figure 5F.

Amot promotes actin filament formation at focal adhesions

Next, we verified the BioID data by co-immunoprecipitation (coIP) analysis. As Amot depletion negatively affects EC migration, we performed the IP analysis at 40% and 100% confluency. The steady-state levels of the components of the focal adhesion adhesome remained unchanged as shown by WB (Figure 6A). Interestingly, the association of Amot to actin and focal adhesion proteins was readily detected in sub-confluent cells but largely lost when cells were confluent (Figure 6A). The association of Amot, as well as actin and Vinculin, was also verified by Kank2 and Zyxin pull-down (Figures S6A and S6B).

To verify the influence on integrins, we harvested protein lysates from control-siRNA- and Amot-siRNA-treated BAE cells. Interestingly, both $\alpha v\beta 3$ and $\beta 1$ integrins bound specifically to p130-Amot, thus arguing that the interaction is mediated by the N-terminal domain (Figures 6B and 6C). The IP of Talin revealed a similar Amot isoform preference (Figure 6D).

Our data indicated that Amot did not bind actin under confluent conditions. Furthermore, depletion of Amot did not affect the association of Talin or Vinculin to $av\beta 3$ and $\beta 1$ integrins (Figures 6B and 6C). However, the IP of $\alpha v\beta 3$ in Amot-depleted cells resulted in less binding of actin (75% reduction) even though steady-state levels remained unchanged (Figure 6B; Figures S6C and S6D).

We hypothesized that Amot may affect the association or polymerization of actin filaments in response to integrin activation. To compare the focal adhesion organization in BAE cells transfected with control or Amot siRNA, we plated individual cells on Y-shaped Fn-coated CYTOO chips. Amot depletion did not affect the recruitment of Vinculin to sites of focal adhesion, whereas the intensity of actin staining was significantly decreased (Figure 6E; quantification in Figures 6F and 6G). The observed reduced actin filament formation in *amot*-depleted cells was not due to differences in dynamics in cell spreading. Cell attachment and spreading were analyzed by using an IncuCyte live-cell analysis system. Both control and Amot-depleted cells showed similar kinetics during 6 h after cell plating (Figures S6E and S6F). Taken together, we present evidence that Amot is a component of the integrin adhesome in ECs where under pro-migratory or sub-confluent conditions promote actin filament formation (hypothetic schematic in Figure 6H).

Amot is required for tumor angiogenesis

The ECM of tumors is heterogenous, and the composition varies depending on tumor origin and subtype. This may explain why endothelial-specific inactivation of Fn and $\alpha 5$ and αv integrin severely affects developmental angiogenesis and causes lethality *in utero* but has little effect on tumor angiogenesis in the adult stage (Murphy et al., 2015). As we observed the expression of Amot in blood vessels of human tumors, we investigated whether Amot is also implicated in tumor angiogenesis. For this purpose, we studied pathological angiogenesis in the tumor model with Lewis lung carcinoma (LLC) transplantation and in the transgenic mouse model of breast cancer MMTV-PyMT. The LLC model has been used extensively to assess the efficacy of anti-angiogenic therapies. Mice were injected with tamoxifen 2 weeks before and after subcutaneous injection with LLC cells (diagram in Figure 7A) to provide either an $amot^{ec+}$ or $amot^{ec-}$ environment for tumor growth. As shown in Figure 7B, LLC tumors from $amot^{ec-}$ animals were significantly smaller as assessed by tumor weight (Figure 7C). Immunostaining of sections from resected tumors showed a marked decrease in vascular density and an increased percentage of necrosis in $amot^{ec-}$ tumors compared with $amot^{ec+}$ (Figures 7D and 7E).

Figure 4. Amot relays force between matrix and EC

(A) IF staining of IB4 (in red) and GFAP (in green) in retinas from $amot^{ec+}$ and $amot^{ec-}$ mice at P6. Radial GFAP staining patterns in an area of interaction between astrocytes and ECs are indicated by the white box in the $amot^{ec+}$ retina. A similar structure was not found in $amot^{ec-}$ retinas. Boxed areas are shown in higher magnification in the right panel.

(B) IF staining of Fn was visualized by enhanced-resolution confocal microscopy. Black arrows in $amot^{ec+}$ tip cell position highlight strained Fn fibrils, and green arrows indicate non-directional and relaxed fibrils in $amot^{ec-}$ retinas.

(C) IF staining analyzing the ratio of strained versus total Fn in a P6 retina of an *amot* floxed mouse injected with tamoxifen. The ROSA26-EYFP (YFP) marker was used to trace recombined ECs (as shown in green). The H5 (H5-myc single-chain antibody) detects strained Fn (as shown in red), whereas Pan-Fn that binds relaxed and strained Fn is shown in magenta. Heatmap images illustrate the ratio of strained versus total Fn.

(D) Representative images from traction force microscopy (TFM) experiments. Left panel shows bright field images of single MS1 cells plated on a 5-kPa polyacrylamide gel homogenously covered with Fn with the superimposed force vector map. The length and orientation of the red pixels indicate the magnitude and directions of exerted traction forces. Stress magnitude was denoted in color scale in Pascal (Pa; right panel). Brighter signals indicate higher force. One pixel is equal to 0.144 μm.

(E) Boxplot showing contractile energy generated by individual cells from control and Amot-siRNA-depleted cells ($n \geq 40$ in each group).

(F) Quantification of the cellular length-to-width ratio on the Fn-coated substratum. *$p < 0.05$; **$p < 0.005$. Scale bars, 50 μm (A–C). See also Figure S4.

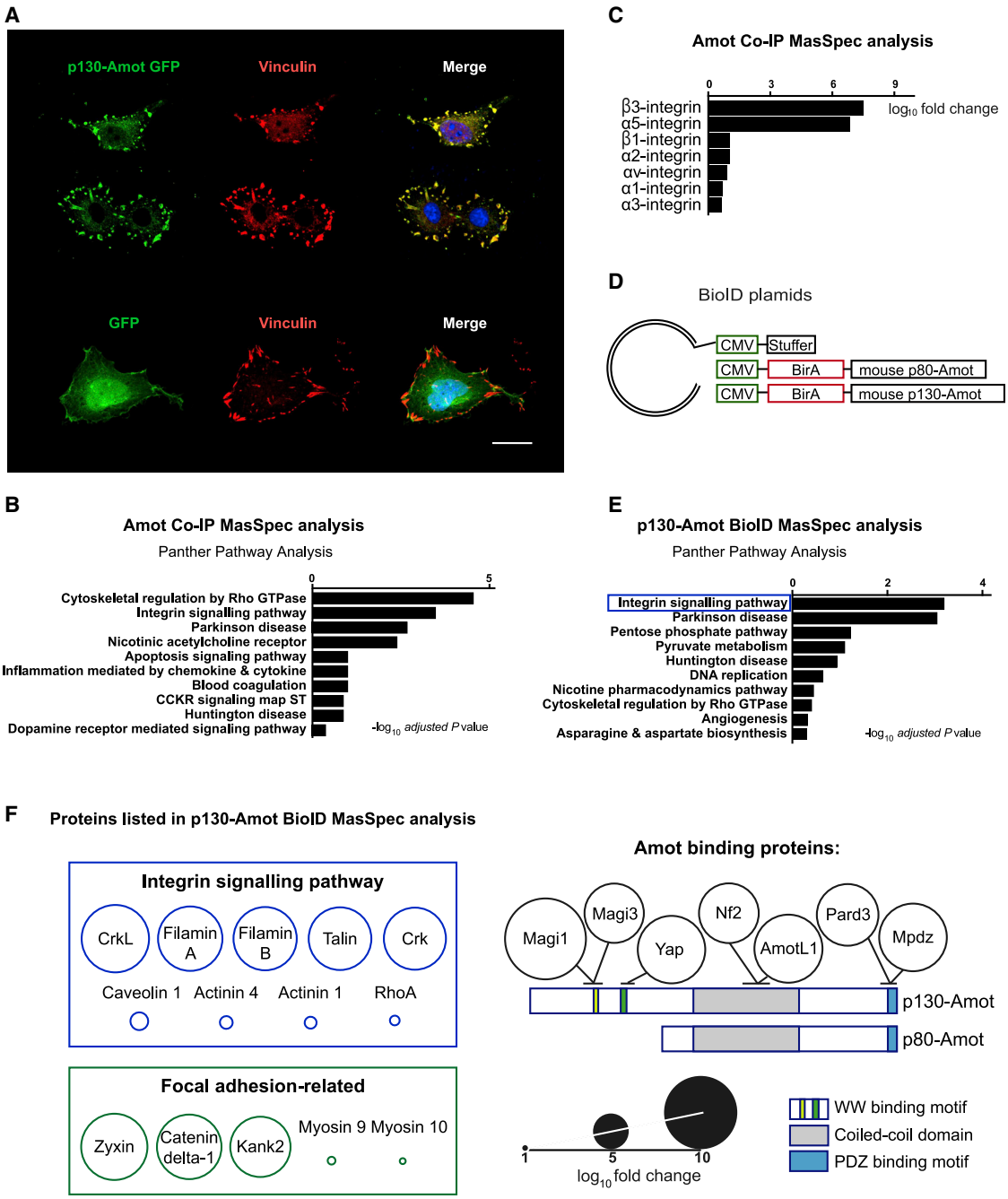

Figure 5. Amot is part of the integrin adhesome

(A) IF image showing the localization of GFP-tagged p130-Amot (in green) and Vinculin (in red). The MS1 cells were transfected by p130-Amot-GFP plasmids (top panel) or GFP plasmid alone as a negative control (bottom panel). Scale bar, 20 μm.

(B) Panther pathway analysis of proteins that were co-immunoprecipitated (coIP) with Amot antibodies. Protein lysates were harvested from the BAE cells cultured to 40% confluency for coIP by using rabbit immunoglobulin G (IgG) (n = 3) and Amot antibodies (n = 2). For each protein, fold change (fc) was calculated, and the ranking is based on positive $\log_{10}$ (fc) values, listed in Table S1.

(C) Integrin subtypes identified as binding partners by MS analysis, which is ranked by $\log_{10}$ (adjusted p value). See also Table S1.

(D) Schematic illustrating the BioID plasmids used for lentivirus particle construction and subsequent transfection for BioID experiments.

(E) The bar diagram showing the top 10 pathways enriched among proteins biotinylated by the BirA p130-Amot construct (n = 178) as identified by MS analysis in MS1 cells (fc of >0). MS analysis included *empty vector* (+/− biotin), *p80-Amot BioID ± biotin*, and *p130-Amot BioID ± biotin*. Fc was calculated as the subtraction value of average quantity detected in control groups (*empty vector ± biotin*, *p130-* and *p80-Amot BioID-biotin)* from the *p130-Amot BioID +biotin* group. The ranking was based on positive $\log_{10}$ (fc) values listed in Table S3.

(legend continued on next page)

Next, we used the MMTV-PyMT mice, in which a Polyoma Middle-T oncogene driven by the MMTV promoter rendered multiple-site breast tumor occurrence at around 8–9 weeks of age (Lin et al., 2003). We crossed *amot*$^{ec-}$ mice into the MMTV-PyMT background and induced *amot*-endothelial-specific depletion at week 4 by tamoxifen injection. An analysis of early-onset tumor occurrence showed 6 weeks longer latency on average in *amot*$^{ec-}$ mice than that in *amot*$^{ec+}$ mice, confirming the protective effect of *amot* deletion on tumor incidence by inhibiting angiogenesis (Figure 7F). Furthermore, the overall survival was significantly improved in *amot*-ablated mice (Figure 7G).

DISCUSSION

In this report, we show that Amot is a part of the integrin adhesome and is essential in relaying force between the ECM and the cellular cytoskeleton. Furthermore, disruption of this relationship by EC-specific gene deletion of Amot resulted in inhibition of both normal and pathological angiogenesis, highlighting the importance of Amot in maintaining normal and pathological transmission of forces in vascular expansion.

Early work by Ingber and Folkman showed that mechanical interactions between ECs and ECM regulated capillary development *in vitro* (Ingber and Folkman, 1989). This led to findings that ECM properties, such as matrix stiffness, control cell shape and function by modulating the cytoskeletal network (Ingber et al., 1995). The forces transmitted through the integrins are in the picomolar range and involve integrin clustering and the formation of a mechanosensory adhesome. This adhesome involves the integrin-binding protein Talin that relays force by unfolding subdomains and exposing cryptic protein interaction sites. In total, the integrin adhesome is highly complex and involvEs over 200 proteins that have been implicated in the cell-ECM interaction (Horton and Humphries, 2016). Our data provide evidence that Amot is a yet undescribed component of the integrin adhesome. Despite the intense research focusing on the mechanotransduction of cell-matrix adhesions, the role of Amot in force transmission has not been described. This may be explained in cellular adhesion studies typically involve fibroblasts that lack Amot expression. Indeed, our studies show that in mouse and humans, Amot is primarily expressed in ECs during developmental angiogenesis as well as in tumor angiogenesis. Recent reports have also shown that Amot is expressed in cells of the inner cell mass of the blastocyst; it controls cellular differentiation here and in the developing neural system (Leung and Zernicka-Goetz, 2013). The development of the neural system is quite reminiscent of the fractal patterning of the retina. Amot inactivation in neural cells of the developing mouse brain also affects cellular branching. In the neural system, Amot triggers the actin filament formation and thereby stabilizes dendritic spines (Wigerius and Quinn, 2018; Rojek et al., 2019). The dynamic interaction between ECM and integrins is also essential for developmental processes such as vascular expansion. Gerhard and coworkers showed that genetic inactivation of Fn in astrocytes of the postnatal retina inhibited endothelial migration as well interfered with filopodial alignment with astrocytic ECM (Stenzel et al., 2011). The major Fn receptor in the retinal endothelium is $\alpha5\beta1$. EC inactivation of the $\beta1$ subunit also has a migratory defect and is essential for the extension of vascular sprouts in the vascular leading edge (Yamamoto et al., 2015). Similar to the *amot*$^{ec-}$, the vascular plexus was condensed most likely due to a lack migration and vessel network expansion. The binding of Amot to focal-adhesion-related proteins such as Talin and Zyxin together with traction force microscopy data indicates a role of Amot not only as part of the integrin adhesome but also as an intracellular force transductor.

We have previously shown that Amot not only binds actin but also triggers the formation of actin filaments (Ernkvist et al., 2006). Supporting this finding, actin and actin-associated proteins were also identified in the BioID MS analysis. The Rho-GTPase RhoA was further shown to bind to Amot that is in line with our findings that the Amot protein complex is required to localize RhoA activity to the leading front of ECs *in vitro* (Ernkvist et al., 2009). Indeed, Amot has been reported to control Rho-GAP activity that may explain the extensive formation of actin fibers upon p130-Amot overexpression (Ernkvist et al., 2006). Furthermore, in migrating ECs, Amot is required for the spatially restricted Rho-GTPase to cellular protrusions or lamellipodia as shown by Rho-FRET analysis (Ernkvist et al., 2009). Amot may also mediate cytoskeleton reorganization by activation of other GTPases. Amot has been proposed to orchestrate directional migration as part of the Merlin-Amot-Rich1 protein complex (Das et al., 2015). Furthermore, binding of Amot may also hydrolyze and downregulate the activity of the Rho GTPases Rac1 and cdc42 (Wells et al., 2006, Yi et al., 2011). How the Amot together with the mentioned Rho GTPases work together to orchestrate the actin dynamics during EC migration is still not clear.

The HIPPO pathway effectors Yap and its paralog Taz are both transcriptional factors that have been implicated in mediating mechano-signaling from the cellular environment. Piccolo and coworkers have shown that the transmission of force by the cytoskeleton is a major activator of Yap transcription (Dupont et al., 2011). Of interest in this context is that Yap contains a WW binding motif and interacts with the L/PPXY site Amot. Whether or not Amot is a negative or positive regulator of Yap activity is a matter of controversy. It has been proposed that Amot negatively regulates Yap activity by at least two different pathways, namely, one by cytoplasmic retention and the second by activating Lats1 kinase activity that phosphorylates Yap and thus prevents nuclear translocation. In contrast, Amot has also been shown to promote epithelial and RCC cell migration by promoting Yap nuclear localization and activation of target genes (Lv et al., 2016). Furthermore, deletion of Amot in neurons *in vivo* did not affect transcription of Yap target genes (Rojek et al., 2019). Further studies are required to elucidate in more detail how Amot and Yap interact to promote angiogenesis *in vivo*.

Taken together, our data point to a role of Amot in integrating mechanical cues sensed by the migrating endothelium that is

(F) Proteins identified from BioID-MS analysis. Focal-adhesion-related proteins identified by the Panther integrin signaling pathway is presented in the blue square. The green square shows the focal adhesion proteins that are not part of the Panther integrin pathway grouping. Circle sizes indicate $\log_{10}$ (fc) values. The BioID strategy identified seven known Amot binders, which are presented at the right side. See also Figure S5 and Tables S1–S4.

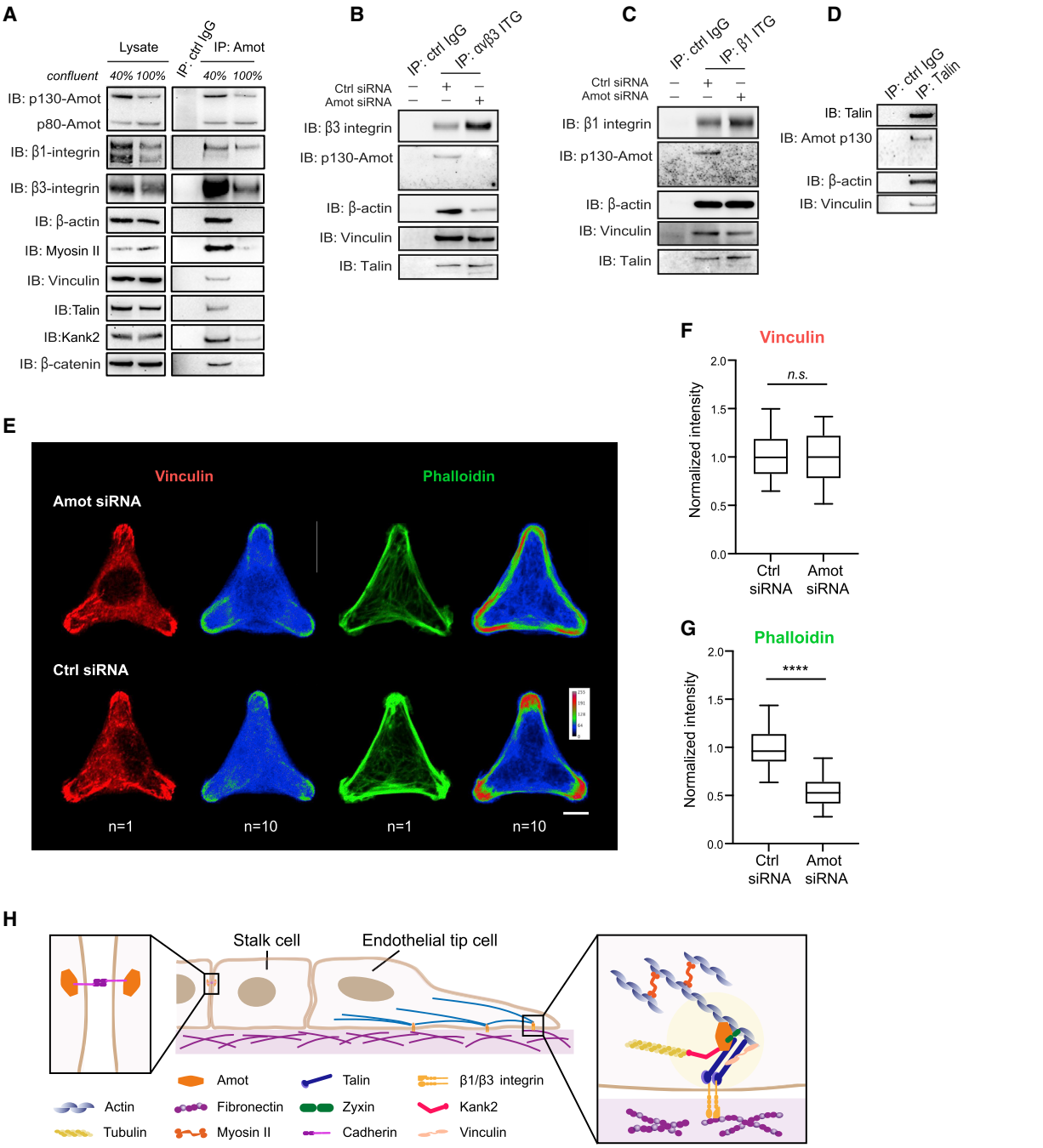

Figure 6. Amot promotes actin filament formation at focal adhesions

(A) CoIP analysis of Amot association to the integrin adhesome. Steady-state levels of integrin and focal adhesion proteins were analyzed by WB in lysates of BAE cells grown at 40% and 100% confluency. Amot was immunoprecipitated in parallel and subjected to WB analysis with the antibodies indicated in the figure.

(B and C) WB analysis of IP using αvβ3-integrin antibody (B) and β1-integrin antibody (C) in BAE cells transfected by control or Amot siRNA.

(D) CoIP and WB analysis of the interaction of Amot with Talin. Three independent experiments were performed for all IP experiments.

(E) Control or Amot-siRNA-depleted BAE cells were plated on Y-shaped CYTOO chips for 4 h. Cells were stained with antibodies against Vinculin (in red), and actin was visualized by phalloidin staining (green). Images of an overlay of 10 cells are also shown. Scale bar, 10 μm.

(F and G) The intensities of Vinculin and phalloidin signals at three vertexes of the Y-shape chips were measured and normalized to the signaling at the central area within the same cell. *n.s.*, not significant; ****$p < 0.0001$.

(H) Hypothetical schematic of focal adhesions where Amot links the actin filaments to Fn in the ECM through the integrin-associated adhesive complex in migratory endothelial tip cells. See also Figure S6.

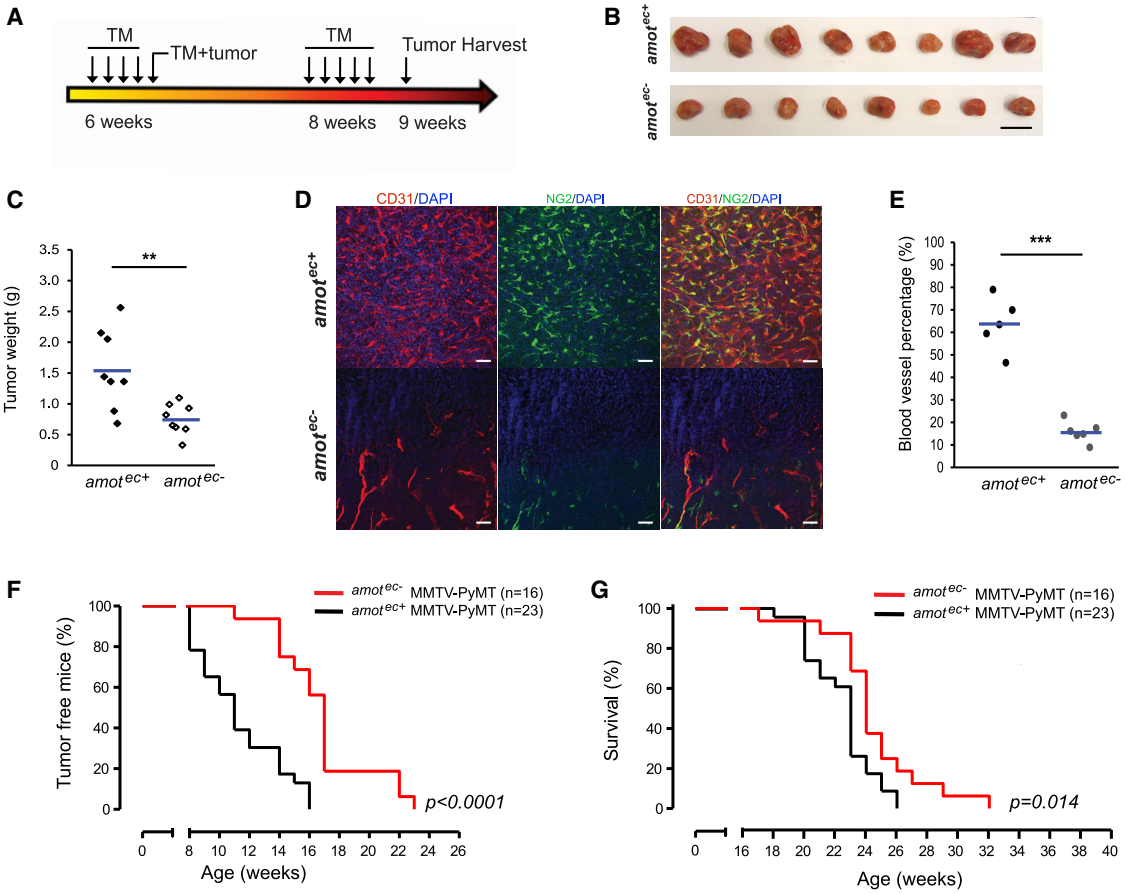

Figure 7. Abrogation of endothelial Amot inhibits tumor growth in transplantation and transgenic tumor mouse models

(A) Schematic of experimental procedure. Tamoxifen injections were performed in *amot*$^{ec-}$ mice at 6 weeks. Lewis lung carcinoma (LLC) tumor cells were injected with tamoxifen together at 8 weeks. LLC tumors were harvested when the largest tumor reached a maximal diameter of 10 mm.

(B) Representative allografted tumors dissected from *amot*$^{ec+}$ (n = 8) and *amot*$^{ec-}$ (n = 8) mice. Scale bar, 10 mm.

(C) Dotplot analysis of tumor weight in *amot*$^{ec+}$ (n = 8) and *amot*$^{ec-}$(n = 8) tumors.

(D) IF staining of LLC tumor vibratome sections (100 μm thick) by anti-CD31 (in red) and anti-NG2 (in green) antibodies. Note the lower blood vessel density of the *amot*$^{ec-}$ tumor. Nuclei were visualized by DAPI (in blue). Scale bars, 50 μm.

(E) Analysis of blood vessel coverage by quantification of CD31 staining on cryosection of *amot*$^{ec+}$ (n = 5) and *amot*$^{ec-}$ (n = 6) tumors.

(F) Analysis of breast tumor incidence in MMTV-PyMT mice with *amot*$^{ec-}$ (n = 16) and *amot*$^{ec+}$ (n = 23).

(G) Kaplan-Meier survival curves of *amot*$^{ec+}$ MMTV-PyMT (black line, n = 23) and *amot*$^{ec-}$ mice (red line, n = 16). The interval omitted is from the 2nd–16th week.

**p < 0.005; ***p < 0.001.

translated to actomyosin contractility and required for EC migration. The observed functions of Amot in both vessel and neuronal networks suggest that a similar mechanism may be in place for other migratory processes such as the formation of branching networks of other organs.

STAR★METHODS

Detailed methods are provided in the online version of this paper and include the following:

- KEY RESOURCES TABLE
- RESOURCE AVAILABILITY
  - Lead contact
  - Materials availability
  - Data and code availability
- EXPERIMENTAL MODEL AND SUBJECT DETAILS
  - Mice
  - Cell lines and primary cells
- METHOD DETAILS
  - Mice treatment
  - Transient transfection for knockdown and overexpression
  - Proximity biotinylation (BioID)
  - Immunofluorescence (IF) staining
  - H5-myc single-chain variable fragment (scFv) antibody
  - Traction force microscopy (TFM)
  - Western blot (WB) analysis and Co-immunoprecipitation (Co-IP)
  - Mass spectrometry (MS) sample preparation
  - LC-MS/MS analysis and peptide/protein identification
- QUANTIFICATION AND STATISTICAL ANALYSIS

SUPPLEMENTAL INFORMATION

Supplemental information can be found online at https://doi.org/10.1016/j.celrep.2021.109616.

ACKNOWLEDGMENTS

We thank Dr. Akihiko Shimono, National University of Singapore, for sharing Amot^{floxed} conditional knockout mouse and Dr. Ralf H. Adams from University of Münster for the Cdh5(PAC)^{CreERT2} and ROSA26-EYFP transgenic mice. Mass spectrometry analysis was performed by the Clinical Proteomics Mass Spectrometry facility, Karolinska Institutet/Karolinska University Hospital/Science for Life Laboratory.

This study was supported by the following grants: Swedish Cancer Society, the Swedish Childhood Cancer Foundation, Cancer Society of Stockholm and the Swedish Research Council, The Swedish Heart and Lung Society, Cancer and Allergy Foundation, Knut and Alicia Wallenberg Foundation (Yuanyuan Zhang, S.K., Y. Zheng, Yumeng Zhang, D.K.-C.C., and L.H.); PhD scholarship (no. 2011622044/201808130149) from Chinese Scholarship Council (Yuanyuan Zhang, Yumeng Zhang); grants from Uehera Memorial Foundation in Japan (S.K.); grants of Fondazione Ricerca Molinette Onlus 8893/5 and Italian Association for Cancer Research - IG 11675 (G.B. and F.C.); Iris, Stig och Gerry Castenbäcks Stiftelse for Cancer Research (N.P.T.); and grant ANR-17-CE30-0032-01(K.H. and M.B.).

AUTHOR CONTRIBUTIONS

Yuanyuan Zhang wrote the manuscript, maintained the Amot conditional KO mouse model, performed experiments and data analysis, drew schematics, and finalized all figures. Yumeng Zhang and S.K. helped with mouse handling and the performed experiment and data analysis. Y. Zheng established the Amot conditional KO mouse model and performed experiments and data analysis. G.B. and F.C. backcrossed PyMT tumor-prone mice with *amot*$^{ec+}$ mice to generate *amot*$^{ec+}$/PyMT and *amot*$^{ec-}$/PyMT mice. G.B., J.N., K.H., D.C., M.B., and T.H.B. performed the experiment and data analysis. L.H. contributed to design experiments and manuscript writing. All authors reviewed the manuscript prior to submission.

DECLARATION OF INTERESTS

The authors declare no competing financial interests.

Received: February 2, 2021
Revised: June 7, 2021
Accepted: August 5, 2021
Published: August 24, 2021

REFERENCES

Aase, K., Ernkvist, M., Ebarasi, L., Jakobsson, L., Majumdar, A., Yi, C., Birot, O., Ming, Y., Kvanta, A., Edholm, D., et al. (2007). Angiomotin regulates endothelial cell migration during embryonic angiogenesis. Genes Dev. *21*, 2055–2068.

Baneyx, G., Baugh, L., and Vogel, V. (2002). Fibronectin extension and unfolding within cell matrix fibrils controlled by cytoskeletal tension. Proc. Natl. Acad. Sci. USA *99*, 5139–5143.

Bondzie, P.A., Chen, H.A., Cao, M.Z., Tomolonis, J.A., He, F., Pollak, M.R., and Henderson, J.M. (2016). Non-muscle myosin-IIA is critical for podocyte f-actin organization, contractility, and attenuation of cell motility. Cytoskeleton (Hoboken) *73*, 377–395.

Bratt, A., Wilson, W.J., Troyanovsky, B., Aase, K., Kessler, R., Van Meir, E.G., and Holmgren, L. (2002). Angiomotin belongs to a novel protein family with conserved coiled-coil and PDZ binding domains. Gene *298*, 69–77.

Butler, J.P., Tolić-Nørrelykke, I.M., Fabry, B., and Fredberg, J.J. (2002). Traction fields, moments, and strain energy that cells exert on their surroundings. Am. J. Physiol. Cell Physiol. *282*, C595–C605.

Cao, L., Nicosia, J., Larouche, J., Zhang, Y., Bachman, H., Brown, A.C., Holmgren, L., and Barker, T.H. (2017). Detection of an Integrin-Binding Mechanoswitch within Fibronectin during Tissue Formation and Fibrosis. ACS Nano *11*, 7110–7117.

Chen, E.Y., Tan, C.M., Kou, Y., Duan, Q., Wang, Z., Meirelles, G.V., Clark, N.R., and Ma'ayan, A. (2013). Enrichr: interactive and collaborative HTML5 gene list enrichment analysis tool. BMC Bioinformatics *14*, 128.

Dallas, S.L., Sivakumar, P., Jones, C.J., Chen, Q., Peters, D.M., Mosher, D.F., Humphries, M.J., and Kielty, C.M. (2005). Fibronectin regulates latent transforming growth factor-beta (TGF beta) by controlling matrix assembly of latent TGF beta-binding protein-1. J. Biol. Chem. *280*, 18871–18880.

Das, T., Safferling, K., Rausch, S., Grabe, N., Boehm, H., and Spatz, J.P. (2015). A molecular mechanotransduction pathway regulates collective migration of epithelial cells. Nat. Cell Biol. *17*, 276–287.

Dupont, S., Morsut, L., Aragona, M., Enzo, E., Giulitti, S., Cordenonsi, M., Zanconato, F., Le Digabel, J., Forcato, M., Bicciato, S., et al. (2011). Role of YAP/TAZ in mechanotransduction. Nature *474*, 179–183.

Eilken, H.M., and Adams, R.H. (2010). Dynamics of endothelial cell behavior in sprouting angiogenesis. Curr. Opin. Cell Biol. *22*, 617–625.

Ernkvist, M., Aase, K., Ukomadu, C., Wohlschlegel, J., Blackman, R., Veitonmäki, N., Bratt, A., Dutta, A., and Holmgren, L. (2006). p130-angiomotin associates to actin and controls endothelial cell shape. FEBS J. *273*, 2000–2011.

Ernkvist, M., Luna Persson, N., Audebert, S., Lecine, P., Sinha, I., Liu, M., Schlueter, M., Horowitz, A., Aase, K., Weide, T., et al. (2009). The Amot/Patj/Syx signaling complex spatially controls RhoA GTPase activity in migrating endothelial cells. Blood *113*, 244–253.

Folkman, J. (1995). Angiogenesis in cancer, vascular, rheumatoid and other disease. Nat. Med. *1*, 27–31.

Fruttiger, M. (2007). Development of the retinal vasculature. Angiogenesis *10*, 77–88.

Fruttiger, M., Calver, A.R., Krüger, W.H., Mudhar, H.S., Michalovich, D., Takakura, N., Nishikawa, S., and Richardson, W.D. (1996). PDGF mediates a neuron-astrocyte interaction in the developing retina. Neuron *17*, 1117–1131.

Geiger, B., Bershadsky, A., Pankov, R., and Yamada, K.M. (2001). Transmembrane crosstalk between the extracellular matrix-cytoskeleton crosstalk. Nat. Rev. Mol. Cell Biol. *2*, 793–805.

Gerhardt, H., and Betsholtz, C. (2005). How do endothelial cells orientate? EXS, 3–15.

Gerhardt, H., Golding, M., Fruttiger, M., Ruhrberg, C., Lundkvist, A., Abramsson, A., Jeltsch, M., Mitchell, C., Alitalo, K., Shima, D., and Betsholtz, C. (2003). VEGF guides angiogenic sprouting utilizing endothelial tip cell filopodia. J. Cell Biol. *161*, 1163–1177.

Hildebrand, S., Hultin, S., Subramani, A., Petropoulos, S., and Zhang, Y. (2017). The E-cadherin/AmotL2 complex organizes actin filaments required for epithelial hexagonal packing and blastocyst hatching. Sci. Rep. *7*, 9540.

Horton, E.R., and Humphries, J.D. (2016). The integrin adhesome network at a glance. J. Cell Sci. *129*, 4159–4163.

Hughes, C.S., Foehr, S., Garfield, D.A., Furlong, E.E., Steinmetz, L.M., and Krijgsveld, J. (2014). Ultrasensitive proteome analysis using paramagnetic bead technology. Mol. Syst. Biol. *10*, 757.

Hultin, S., Zheng, Y., Mojallal, M., Vertuani, S., Gentili, C., Balland, M., Milloud, R., Belting, H.G., Affolter, M., Helker, C.S., et al. (2014). AmotL2 links VE-cadherin to contractile actin fibres necessary for aortic lumen expansion. Nat. Commun. *5*, 3743.

Hynes, R.O. (2002). Integrins: bidirectional, allosteric signaling machines. Cell *110*, 673–687.

Ingber, D.E., and Folkman, J. (1989). Mechanochemical switching between growth and differentiation during fibroblast growth factor-stimulated angiogenesis in vitro: role of extracellular matrix. J. Cell Biol. *109*, 317–330.

Ingber, D.E., Prusty, D., Sun, Z., Betensky, H., and Wang, N. (1995). Cell shape, cytoskeletal mechanics, and cell cycle control in angiogenesis. J. Biomech. *28*, 1471–1484.

Jiang, B., Liou, G.I., Behzadian, M.A., and Caldwell, R.B. (1994). Astrocytes modulate retinal vasculogenesis: effects on fibronectin expression. J. Cell Sci. *107*, 2499–2508.

Klotzsch, E., Smith, M.L., Kubow, K.E., Muntwyler, S., Little, W.C., Beyeler, F., Gourdon, D., Nelson, B.J., and Vogel, V. (2009). Fibronectin forms the most extensible biological fibers displaying switchable force-exposed cryptic binding sites. Proc. Natl. Acad. Sci. USA *106*, 18267–18272.

Kuleshov, M.V., Jones, M.R., Rouillard, A.D., Fernandez, N.F., Duan, Q., Wang, Z., Koplev, S., Jenkins, S.L., Jagodnik, K.M., Lachmann, A., et al. (2016). Enrichr: a comprehensive gene set enrichment analysis web server 2016 update. Nucleic Acids Res. *44*, W90–W97.

Leiss, M., Beckmann, K., Girós, A., Costell, M., and Fässler, R. (2008). The role of integrin binding sites in fibronectin matrix assembly in vivo. Curr. Opin. Cell Biol. *20*, 502–507.

Lemmon, C.A., Chen, C.S., and Romer, L.H. (2009). Cell traction forces direct fibronectin matrix assembly. Biophys. J. *96*, 729–738.

Leung, C.Y., and Zernicka-Goetz, M. (2013). Angiomotin prevents pluripotent lineage differentiation in mouse embryos via Hippo pathway-dependent and -independent mechanisms. Nat. Commun. *4*, 2251.

Levchenko, T., Aase, K., Troyanovsky, B., Bratt, A., and Holmgren, L. (2003). Loss of responsiveness to chemotactic factors by deletion of the C-terminal protein interaction site of angiomotin. J. Cell Sci. *116*, 3803–3810.

Lin, E.Y., Jones, J.G., Li, P., Zhu, L., Whitney, K.D., Muller, W.J., and Pollard, J.W. (2003). Progression to malignancy in the polyoma middle T oncoprotein mouse breast cancer model provides a reliable model for human diseases. Am. J. Pathol. *163*, 2113–2126.

Lv, M., Li, S., Luo, C., Zhang, X., Shen, Y., Sui, Y.X., Wang, F., Wang, X., Yang, J., Liu, P., and Yang, J. (2016). Angiomotin promotes renal epithelial and carcinoma cell proliferation by retaining the nuclear YAP. Oncotarget *7*, 12393–12403.

Mandal, K., Wang, I., Vitiello, E., Orellana, L.A., and Balland, M. (2014). Cell dipole behaviour revealed by ECM sub-cellular geometry. Nat. Commun. *5*, 5749.

Maruthamuthu, V., Sabass, B., Schwarz, U.S., and Gardel, M.L. (2011). Cell-ECM traction force modulates endogenous tension at cell-cell contacts. Proc. Natl. Acad. Sci. USA *108*, 4708–4713.

Murphy, P.A., Begum, S., and Hynes, R.O. (2015). Tumor angiogenesis in the absence of fibronectin or its cognate integrin receptors. PLoS One *10*, e0120872.

Pankov, R., and Yamada, K.M. (2002). Fibronectin at a glance. J. Cell Sci. *115*, 3861–3863.

Pitulescu, M.E., Schmidt, I., Benedito, R., and Adams, R.H. (2010). Inducible gene targeting in the neonatal vasculature and analysis of retinal angiogenesis in mice. Nat. Protoc. *5*, 1518–1534.

Potente, M., Gerhardt, H., and Carmeliet, P. (2011). Basic and therapeutic aspects of angiogenesis. Cell *146*, 873–887.

Rahikainen, R., Öhman, T., Turkki, P., Varjosalo, M., and Hytönen, V.P. (2019). Talin-mediated force transmission and talin rod domain unfolding independently regulate adhesion signaling. J. Cell Sci. *132*, jcs226514.

Rojek, K.O., Krzemień, J., Doleżyczek, H., Boguszewski, P.M., Kaczmarek, L., Konopka, W., Rylski, M., Jaworski, J., Holmgren, L., and Prószyński, T.J. (2019). Amot and Yap1 regulate neuronal dendritic tree complexity and locomotor coordination in mice. PLoS Biol. *17*, e3000253.

Roux, K.J., Kim, D.I., Burke, B., and May, D.G. (2018). BioID: A Screen for Protein-Protein Interactions. Curr. Protoc. Protein Sci. *91*, 19.23.1–19.23.15.

Schiller, H.B., Friedel, C.C., Boulegue, C., and Fässler, R. (2011). Quantitative proteomics of the integrin adhesome show a myosin II-dependent recruitment of LIM domain proteins. EMBO Rep. *12*, 259–266.

Schwartz, M.A. (2010). Integrins and extracellular matrix in mechanotransduction. Cold Spring Harb. Perspect. Biol. *2*, a005066.

Smith, M.A., Blankman, E., Gardel, M.L., Luettjohann, L., Waterman, C.M., and Beckerle, M.C. (2010). A zyxin-mediated mechanism for actin stress fiber maintenance and repair. Dev. Cell *19*, 365–376.

Srinivas, S., Watanabe, T., Lin, C.S., William, C.M., Tanabe, Y., Jessell, T.M., and Costantini, F. (2001). Cre reporter strains produced by targeted insertion of EYFP and ECFP into the ROSA26 locus. BMC Dev. Biol. *1*, 4.

Stahl, A., Connor, K.M., Sapieha, P., Chen, J., Dennison, R.J., Krah, N.M., Seaward, M.R., Willett, K.L., Aderman, C.M., Guerin, K.I., et al. (2010). The mouse retina as an angiogenesis model. Invest. Ophthalmol. Vis. Sci. *51*, 2813–2826.

Stenzel, D., Lundkvist, A., Sauvaget, D., Busse, M., Graupera, M., van der Flier, A., Wijelath, E.S., Murray, J., Sobel, M., Costell, M., et al. (2011). Integrin-dependent and -independent functions of astrocytic fibronectin in retinal angiogenesis. Development *138*, 4451–4463.

Sun, Z., Tseng, H.Y., Tan, S., Senger, F., Kurzawa, L., Dedden, D., Mizuno, N., Wasik, A.A., Thery, M., Dunn, A.R., and Fässler, R. (2016). Kank2 activates talin, reduces force transduction across integrins and induces central adhesion formation. Nat. Cell Biol. *18*, 941–953.

Tseng, Q., Wang, I., Duchemin-Pelletier, E., Azioune, A., Carpi, N., Gao, J., Filhol, O., Piel, M., Théry, M., and Balland, M. (2011). A new micropatterning method of soft substrates reveals that different tumorigenic signals can promote or reduce cell contraction levels. Lab Chip *11*, 2231–2240.

Turner, C.J., Badu-Nkansah, K., and Hynes, R.O. (2017). Endothelium-derived fibronectin regulates neonatal vascular morphogenesis in an autocrine fashion. Angiogenesis *20*, 519–531.

Uemura, A., Kusuhara, S., Katsuta, H., and Nishikawa, S. (2006). Angiogenesis in the mouse retina: a model system for experimental manipulation. Exp. Cell Res. *312*, 676–683.

Uhlén, M., Fagerberg, L., Hallström, B.M., Lindskog, C., Oksvold, P., Mardinoglu, A., Sivertsson, Å., Kampf, C., Sjöstedt, E., Asplund, A., et al. (2015). Proteomics. Tissue-based map of the human proteome. Science *347*, 1260419.

Wells, C.D., Fawcett, J.P., Traweger, A., Yamanaka, Y., Goudreault, M., Elder, K., Kulkarni, S., Gish, G., Virag, C., Lim, C., et al. (2006). A Rich1/Amot complex regulates the Cdc42 GTPase and apical-polarity proteins in epithelial cells. Cell *125*, 535–548.

Wigerius, M., and Quinn, D. (2018). The polarity protein Angiomotin p130 controls dendritic spine maturation. J. Cell Biol. *217*, 715–730.

Yamamoto, H., Ehling, M., Kato, K., Kanai, K., van Lessen, M., Frye, M., Zeuschner, D., Nakayama, M., Vestweber, D., and Adams, R.H. (2015). Integrin β1 controls VE-cadherin localization and blood vessel stability. Nat. Commun. *6*, 6429.

Yi, C., Troutman, S., Fera, D., Stemmer-Rachamimov, A., Avila, J.L., Christian, N., Persson, N.L., Shimono, A., Speicher, D.W., Marmorstein, R., et al. (2011). A tight junction-associated Merlin-angiomotin complex mediates Merlin's regulation of mitogenic signaling and tumor suppressive functions. Cancer Cell *19*, 527–540.

Zaidel-Bar, R., and Geiger, B. (2010). The switchable integrin adhesome. J. Cell Sci. *123*, 1385–1388.

Zeng, H., Ortiz, A., Shen, P.F., Cheng, C.J., Lee, Y.C., Yu, G., Lin, S.C., Creighton, C.J., Yu-Lee, L.Y., and Lin, S.H. (2017). Angiomotin regulates prostate cancer cell proliferation by signaling through the Hippo-YAP pathway. Oncotarget *8*, 10145–10160.

Zhang, Q., Magnusson, M.K., and Mosher, D.F. (1997). Lysophosphatidic acid and microtubule-destabilizing agents stimulate fibronectin matrix assembly through Rho-dependent actin stress fiber formation and cell contraction. Mol. Biol. Cell *8*, 1415–1425.

Zheng, Y., Zhang, Y., Barutello, G., Chiu, K., Arigoni, M., Giampietro, C., Cavallo, F., and Holmgren, L. (2016). Angiomotin like-1 is a novel component of the N-cadherin complex affecting endothelial/pericyte interaction in normal and tumor angiogenesis. Sci. Rep. *6*, 30622.

Zhong, C., Chrzanowska-Wodnicka, M., Brown, J., Shaub, A., Belkin, A.M., and Burridge, K. (1998). Rho-mediated contractility exposes a cryptic site in fibronectin and induces fibronectin matrix assembly. J. Cell Biol. *141*, 539–551.

STAR★METHODS

KEY RESOURCES TABLE

REAGENT or RESOURCE	SOURCE	IDENTIFIER
Antibodies		
GFP	Abcam	Cat# ab13970; RRID:AB_300798
ERG	Abcam	Cat# ab92513; RRID:AB_2630401
GFAP	Dako	Cat# Z0334; RRID:AB_10013382
Fibronectin	Thermo Fisher Scientific	Cat# MA5-11981; RRID:AB_10982280
FAK	Abcam	Cat# ab40794; RRID:AB_732300
Fibronectin	Millipore	Cat# AB2033; RRID:AB_2105702
Paxillin	BD	Cat# 610620; RRID:AB_397952
Kank2	Sigma	Cat# HPA015643; RRID:AB_1844839
Zyxin	Abcam	Cat# ab109316; RRID: N/A
Talin	Abcam	Cat# ab157808; RRID: N/A
Myosin	Cell signaling	Cat# 3672; RRID:AB_10692513
Vinculin	Sigma	Cat# V9131; RRID:AB_477629
β-actin	Abcam	Cat# ab8227; RRID:AB_2305186
GAPDH	Abcam	Cat# ab8245; RRID:AB_2107448
Myc Antibody	Cell signaling	Cat# 2276; RRID:AB_331783
β1 integrin	Genetex	Cat# GTX128839; RRID:AB_2885823
β1 integrin	BD	Cat# 610467; RRID:AB_2128060
β1 integrin (alpha 5)	Millipore	Cat# MAB2514; RRID:AB_94626
β3 integrin (alpha v)	Millipore	Cat# MAB1976; RRID:AB_2296419
β3 integrin	abcam	Cat# ab119992; RRID:AB_10903329
CD31	BD	Cat# 557355; RRID:AB_396660
NG2	Sigma	Cat# 05-710; RRID:AB_309925
BirA	abcam	Cat# ab232732; RRID: N/A
Amot	Innovagen, Lund, Sweden	Purified from rabbit serum
donkey anti-Sheep IgG (H+L) Alexa Fluor® 488 conjugate	Thermo Fisher Scientific	Cat# A-11015; RRID:AB_141362
goat anti-Chicken IgG (H+L) Alexa Fluor® 488 conjugate	Thermo Fisher Scientific	Cat# A-11039; RRID:AB_142924
donkey anti-Goat IgG (H+L) Alexa Fluor® 488 conjugate	Thermo Fisher Scientific	Cat# A-11055; RRID:AB_2534102
chicken anti-Rabbit IgG (H+L) Alexa Fluor® 488 conjugate	Thermo Fisher Scientific	Cat# A-21441; RRID:AB_2535859
goat anti-Rat IgG (H+L) Alexa Fluor® 594 conjugate	Thermo Fisher Scientific	Cat# A-11007; RRID:AB_10561522
donkey anti-Rabbit IgG (H+L) Alexa Fluor® 647 conjugate	Thermo Fisher Scientific	Cat# A-31573; RRID:AB_2536183
goat anti-Mouse IgG (H+L) Cy3®	Thermo Fisher Scientific	Cat# A10521; RRID:AB_2534030
Streptavidin Alexa Fluor® 405 conjugate	Thermo Fisher Scientific	Cat# S32351; RRID: N/A
Streptavidin Alexa Fluor® 488 conjugate	Thermo Fisher Scientific	Cat# S32354; RRID:AB_2315383
Bacterial and virus strains		
Empty vector plasmid (BioID construct)	VectorBuilder	VB190314-1055uyu pLV[Exp]-Neo-CMV > Stuffer300
mouse p130-Amot BirA-tagged plasmid (BioID construct)	VectorBuilder	VB190414-1109xdu pLV[Exp]-Neo-CMV > {BirA(R118G)}:[NM_153319.3]*

(*Continued on next page*)

Continued

REAGENT or RESOURCE	SOURCE	IDENTIFIER
mouse p80-Amot BirA-tagged plasmid (BioID construct)	VectorBuilder	VB190411-1454njh pLV[Exp]-Neo-CMV > {BirA(R118G)}:[NM_133265.2](G449D)
Biological samples		
The human tissue IHC images	Database: The Human Atlas Protein	Ethical permit: Ups 02-577, #2011/473 https://www.proteinatlas.org/search/amot
Chemicals, peptides, and recombinant proteins		
Phalloidin	Life Technologies	Cat# T7471
Phalloidin	Sigma	Cat# 65906
Phalloidin	Sigma	Cat# P5282
TO-PRO-3	Life Technologies	Cat# T3605
Isolectin B4	VECTOR	Cat# B-1205; RRID:AB_2314661
IgG from rabbit serum	Sigma	Cat# I8140; RRID:AB_1163661
IgG from mouse serum	Sigma	Cat# I8765; RRID:AB_1163672
IgG from rat serum	Sigma	Cat# I8015; RRID:AB_1163629
Tamoxifen	Sigma	Cat# T5648
Protease Inhibitor	Roche	Cat# 4693159001
Paraformaldehyde solution 4% in PBS	ChemCruz	Cat# sc-281692
Blebbistatin	Sigma	Cat# B0560
biotin	Sigma	Cat# B4501
urea	Sigma	Cat# U5378
Critical commercial assays		
RNeasy Mini Kit	QIAGEN	Cat# 74104
EndoFree® Plasmid Maxi Kit	QIAGEN	Cat# 12362
CYTOOCHIPS STARTER'S A X18	CYTOO	Cat# 10-900-00-18
Lipofectamine 3000 Transfection Reagent	Invitrogen	Cat# L3000015
Lipofectamine RNAiMAX Reagent	Thermo Fisher Scientific	Cat# 13778075
Deposited data		
Original blots for WB	Mendeley Data	https://dx.doi.org/10.17632/k57km66fkd.1
Amot Co-IP Mass Spectrometry analysis (raw file)	Mendeley Data	https://dx.doi.org/10.17632/k57km66fkd.1
p130-Amot Bio-ID Mass Spectrometry analysis (raw file)	Mendeley Data	https://dx.doi.org/10.17632/k57km66fkd.1
Experimental models: Cell lines		
MS1 cells (Mile Sven 1), SV40-transformed mouse endothelial cells	ATCC	CRL.2279
Primary BAE (Bovine Aortic Endothelial) cells	Sigma	B304-05
Experimental models: Organisms/strains		
$Amot^{floxed}$ mouse strain	National University of Singapore	Dr. Akihiko Shimono
$Cdh5(PAC)^{CreERT2}$ and ROSA26-EYFP transgenic mouse strains	University of Münster	Dr. Ralf H. Adams
Oligonucleotides		
ON-TARGETplus control pool non-targeting pool	GE Healthcare Dharmacon	D-001810-10
ON-TARGETplus SMARTpool Mouse Amot	GE Healthcare Dharmacon	L-058986-01
Bovine control siRNA (Customized product)	GE Healthcare Dharmacon	5′-AUUGUAUGCGAUCGCAGA CUU-3′
Bovine Amot siRNA (Customized product)	GE Healthcare Dharmacon	5′-GGAGAAGGCUAUUCCGCU AUU-3′
siGENOME Control Pool	GE Healthcare Dharmacon	1# D-001206-13
Human Amot siRNA (Customized product)	GE Healthcare Dharmacon	5′-AUUGUAUUCUGAAACGUU GGU-3′
Primers for Amot flox/flox, Amot Knockout, CDH5-Cre and YFP reporter	Thermo Fisher Scientific	Details in Table S5

(*Continued on next page*)

Continued		
REAGENT or RESOURCE	SOURCE	IDENTIFIER
Recombinant DNA		
mouse p130-Amot-GFP plasmid	VectorBuilder	VB190414-1114pch pcDNA3.1(+)-EGFP: [NM_153319.3]*
GFP plasmid	Addgene	#129020 pcDNA3.1(+) EGFP
Software and algorithms		
ImageJ	imageJ Software	https://imagej.nih.gov/ij/
Incucyte® Base Analysis Software	IncuCyte	N/A
Adobe Photoshop 2021	Adobe	https://www.adobe.com/
GraphPad Prism 9	GraphPad Software	https://www.graphpad.com/
Microsoft Office Standard 2010	Microsoft Corporation	https://www.microsoft.com/en-us/
Adobe Illustrator 2021	Adobe	https://www.adobe.com/
Other		
Polyacrylamide Bis-Tris 4-12% gradient gel	Novex	Cat# NP0322BOX
Nitrocellulose membrane	Whatman	Cat# 10401396
Fluoroshield with DAPI	Sigma	Cat# F6057
Protein G Sepharose 4 fast flow	GE Healthcare	Cat# 17-0618-01
SDS sample buffer	Novex	Cat# 1225644
Sample reducing agent	Novex	Cat# 1176192
Western Lightning Plus-ECL	PerkinElmer	Cat# 203-170071
RPMI-1640	GIBCO	Cat# 21875-034
Fetal Bovine Serum	GIBCO	Cat# 10270-106
Penicillin/streptomycin (P/S)	GIBCO	Cat# 15140-122
BAE medium	Sigma	Cat# B211-500
DMEM medium	GIBCO	Cat# 41965-039

RESOURCE AVAILABILITY

Lead contact

Further information and requests for resources and reagents can be directed to the lead contact, Lars Holmgren (lars.holmgren@ki.se).

Materials availability

This study did not generate new unique reagents.

Data and code availability

The raw Amot Co-IP mass spectrometry proteomics data and p130-Amot BioID mass spectrometry proteomics data are available in Mendeley Data, as well as the original blots of WB performed in this study (https://dx.doi.org/10.17632/k57km66fkd.1). This study did not generate any unique code. Any additional information required to reanalyze the data reported in this paper is available from the lead contact upon request.

EXPERIMENTAL MODEL AND SUBJECT DETAILS

Mice

The *amot*^{flox} mice, carrying a loxP-flanked *amot* gene, were crossed with Cdh5(PAC)^{CreERT2} and ROSA26-EYFP double transgenic mice. *Amot*$^{ec+}$ and *amot*$^{ec-}$ are the abbreviations used for depicting *amot*^{wt}-Cdh5(PAC)^{CreERT2}-ROSA26-EYFP and *amot*^{flox}-Cdh5(PAC)^{CreERT2}-ROSA26-EYFP mice, respectively, as the *amot* gene localizes to the X chromosome. Mice were also crossed with mice carrying Polyomavirus Middle T under control of the MMTV promoter (MMTV-PyMT) in the animal facility of the Molecular Biotechnology Center (Turin) and treated in conformity with European Guidelines and policies, as approved by the ethical Committee of the University of Torino. All the mice in this report were in C57BL/6 background. Biopsies from mouse tail-tip and ear were used for genotyping of each mouse included in these studies. Postnatal day 6 (P6) and adult mice (4-6 weeks old) were analyzed in this study. Both female and male animals were included. Ethical permission was granted by the North Stockholm Animal Ethical Committee. All animal housing and experiments were carried out in accordance with the guidelines of the Swedish Board of Agriculture.

Cell lines and primary cells

MS1 cells (Mile Sven 1, ATCC CRL.2279), SV40-transformed mouse ECs, were cultured in RPMI-1640 medium supplemented with 10% FBS and 1% penicillin/streptomycin (P/S) at 37°C, 10% CO2 condition. Primary BAE (Bovine Aortic Endothelial) cells purchased from Sigma (B304-05) were cultured in Bovine Endothelial Cell Growth Medium at 37°C, 10% CO2 condition. LLC cells were cultured in DMEM medium supplemented with 10% FBS and 1% P/S. All products mentioned above are listed in Key resources table.

METHOD DETAILS

Mice treatment

1. Tamoxifen administration

Tamoxifen was dissolved in sunflower oil. For retinal angiogenesis study, tamoxifen (400 μg/mouse/day) was administered by intraperitoneal (IP) injection from P1 to P3 and the retinas were harvested at P6. For adult mice (over 4 weeks old), tamoxifen (2 mg/mouse/day) was given for 5 continuous days, and two weeks after, the retinas were dissected and analyzed.

2. Retinal angiogenesis assay

Mouse retinal angiogenesis assay was performed as previously published (Pitulescu et al., 2010; Stahl et al., 2010). In brief, eyeballs were dissected at P6 or adult age (4-6 weeks old). A portion of them was fixed in 4% paraformaldehyde (PFA) for 1.5 hours (1.5 h) before whole-mount immunostaining. For retinal protein analysis, retinas were dissected out from eyeballs freshly and homogenized on ice to extract protein.

3. Tumor allograft model

The $amot^{ec+}$and $amot^{ec-}$ male mice (≥8 mice per group) at 6 weeks of age were injected by tamoxifen to induce *amot* depletion. Lewis lung carcinoma cells (LLC, 0.5 × 10^6/mouse) were injected subcutaneously on the last day of tamoxifen injection. Tumor growth was manually inspected twice per week and tumor volumes were calculated according to the formula: 0.52 × length × width × width (cm^3). Starting from 2 weeks after the first injection, the same dosage of tamoxifen was injected into the tumor-bearing mice for 5 days. When tumors reached the diameter of 10 mm, mice were sacrificed according to the ethical permission.

Transient transfection for knockdown and overexpression

For siRNA transfections, MS1 and BAE cells were seeded the day before transfection in 10 mm culture Petri dishes pre-coated with 0.5% Fn, at 30% confluent. Both control and Amot siRNAs with final concentration of 25 nM were transfected into the cells with Lipofectamine® RNAiMAX Reagent according to the manufacturer's protocol. The cells were re-plated to dishes/slides for either 4 h (CYTOO chip experiments) or 16 h before harvesting at 40% confluent status (sub-confluent). IF staining or WB were processed afterward.

For Amot overexpression studies, MS1 cells were transfected with mouse p130-Amot-GFP or GFP plasmid using Lipofectamine 3000 according to the protocol of the manufacturer. Immunostaining was performed 24 h post-transfection.

Proximity biotinylation (BioID)

BioID expression constructs were created by cloning cDNA fragments encoding mouse p130-Amot or p80-Amot into the destination lentivirus vector to obtain mouse p130-Amot and p80-Amot fused to the N terminus of *E. coli* biotin ligase (BirA). Empty vector with the same backbone was used as the negative control. All constructs were verified by Restriction Enzyme Digestion. BioID constructs were packaged into lentivirus using Lipofectamine 3000 Transfection Reagent according to the protocol of the manufacturer. MS1 cells were used as target cells for lentivirus transfection with 0.5 mg/mL geneticin. Stable transfected cells were cultured in RPMI-1640 medium supplemented with 10% FBS and 0.5 mg/mL geneticin. For BioID analysis, MS1 cells were treated 16 h with 50 μM biotin, followed harvesting in lysis buffer consisting of 50 mM Tris·Cl pH 7.4, 8 M urea, 1 mM DTT supplemented with protease inhibitors. Lysates was supplemented with 1% Triton X-100 before sonication. Biotinylated proteins were purified with Streptavidin beads overnight at 4°C. After five washes with 8 M urea in 50 mM Tris·Cl pH 7.4 and one wash with 50 mM Tris·Cl pH 7.4, beads were resuspended in PBS and ready for WB and MS analysis. Detailed sequencing information is provided in Key resources table.

Immunofluorescence (IF) staining

Cells were fixed by 4% PFA for 10 min at room temperature (RT) and then were permeabilized with 0.1% Triton X-100 for 1 min. After 1 h blocking with 5% horse serum in PBS, cells were incubated with primary antibodies for 2 h followed by Alexa Fluor® conjugated secondary antibodies for 1 h at RT.

Mouse retinal whole-mount staining protocol has been previously described (Pitulescu et al., 2010). In brief, fixed retinas were permeabilized and blocked in PBS containing 0.3% Triton X-100 and 2% BSA at 4°C overnight. Primary antibodies in Pblec buffer (1.0% Triton X-100 plus 0.1 M $MgCl_2$, 0.1 M $CaCl_2$, 0.01 M $MnCl_2$ in PBS) were added to the retina and incubated at 4°C overnight and subsequently incubated with the fluorescent-conjugated secondary antibodies.

Digital images were acquired using a Zeiss LSM 700 confocal microscope/Airyscan-resolution microscopy and analyzed by ImageJ (NIH). All the primary and secondary antibodies used were listed in Key resources table.

H5-myc single-chain variable fragment (scFv) antibody

Conformation-sensitive single-chain antibody clone H5 with myc tag (H5-myc) was developed using phage display against engineered Fn fragments and has previously been shown to detect a force-induced extension in the FnIII9-10 integrin-binding domain (Cao et al., 2017). H5-myc was used as ordinary primary antibody for retinal staining as described above, except with a 2 h RT incubation with Anti-myc antibody for amplifying the signal before secondary antibody addition. Samples were additionally stained with a pan-Fn antibody to control for total Fn in the matrix. To visualize the degree of force-induced Fn unfolding in the matrix, ratiometric images of H5-myc: Pan-Fn was generated using a custom MATLAB program. Images were first gated using Otsu's method, and masked to analyze only regions where both H5-myc and pan-Fn passed the threshold. Fluorescence intensity of the H5-myc signal was then divided by fluorescence intensity of the pan-Fn signal on a pixel-by-pixel basis, and plotted using a heatmap to display the ratiometric values for each pixel, where a higher ratio indicates greater force-induced unfolding of Fn.

Traction force microscopy (TFM)

5 kPa polyacrylamide gels embedded with fluorescent beads (Thermo Fisher Scientific, F8807) were prepared as previously described (Tseng et al., 2011). For quantitative force measurements, MS1 cells, 72 h after siRNA transfection, were trypsinized and seeded as single cells on top of the hydrogel. Images were acquired using an Eclipse Ti inverted microscope (Nikon) with a 60 x oil immersion objective with 1.5 x zoom (Nikon 1.4 NA) and a Zyla sCMOS camera (Andor), both driven by Andor iQ3, as well as a temperature control system set at 37°C. Images of fluorescent beads within the relaxed and stressed hydrogel were taken before and after cell detachment, respectively, and one bright field image of the cell doublet was recorded.

The method used for force calculations on continuous substrates was described previously (Butler et al., 2002; Mandal et al., 2014). All image processing and calculations have been performed in MATLAB. The displacement field was calculated using a combination of particle image velocimetry and single particle tracking. After drift correction, the mean displacement was calculated by cross-correlating corresponding sub-windows (size 9.22 μm) of the stressed and relaxed bead image. Following, single particle tracking within each sub-window was performed, which led to a high spatial resolution and accuracy of the displacement measurements. The final displacement field was obtained on a regular grid of 1.15 μm by linear interpolation. Forces were reconstructed using Fourier transform traction cytometry with zeroth-order regularization. From this, the contractile energy U, which represents the total energy transferred from the cell to the elastic distortion of the substrate, was calculated

contractile energy as follows:

$$Ec = \frac{1}{2}\sum_{i \in cell}\left(T^i{}_x u^i{}_x + T^i{}_y u^i{}_y\right)\sigma^2$$

Western blot (WB) analysis and Co-immunoprecipitation (Co-IP)

Cells were scraped directly from cell culture dishes in lysis buffer (50 mM HEPES buffer, 150 mM NaCl, 1.5 mM $MgCl_2$, 1 mM EGTA, 10% Glycerol, 1% Triton X-100), with 1 x protease inhibitors at 4°C. Mouse retina were dissected, cut into small pieces and then immersed in lysis buffer. Samples were homogenized using a tissue homogenizer (VWR) in order to improve protein extraction. SDS sample buffer containing 10% sample reducing agent was added to cell lysates and proteins were separated in a polyacrylamide Bis-Tris 4%–12% gradient gel and transferred to a nitrocellulose membrane. The membrane was blocked in PBS containing 5% non-fat milk and 0.1% Tween 20 and sequentially incubated with the primary antibody and horseradish peroxidase (HRP) conjugated secondary antibody. Labeled proteins were detected using Western Lightning Plus-ECL.

Cell lysates were pre-treated with protein G Sepharose beads for 1.5 h. 2 μg antibodies or control IgG of the same origin were incubated overnight with agitation. Bound proteins were harvested using protein G beads for 2 h, followed by five consecutive washes with lysis buffer. Protein complexes were further analyzed by WB. Primary/secondary antibodies and reagents used are listed in Key resources table.

Mass spectrometry (MS) sample preparation

IP samples were dissolved in 200 μL lysis buffer (4% SDS, 50 mM HEPES pH 7.6, 1 mM DTT). After heating at 95°C for 5 min and centrifugation at 14,000 g for 15 min, the supernatant was transferred to new tubes. Protein digestion was performed using a modified SP3-protocol (Hughes et al., 2014). In brief, each sample was alkylated with 40 mM chloroacetamide and Sera-Mag SP3 bead mix (20 μL) was transferred into the protein sample together with 100% acetonitrile to a final concentration of 70%. The mix was incubated under rotation at room temperature for 20 min. The mixture was placed on the magnetic rack and the supernatant was discarded, followed by two washes with 70% ethanol and one with 100% acetonitrile. The beads-protein was reconstituted in 100 μL trypsin buffer (50 mM HEPES pH 7.6 and 0.8 μg trypsin) and incubated overnight at 37°C. The eluted samples were dried in a SpeedVac. Approximately 10 μg was suspended in LC mobile phase A and 1 μg was injected on the LC-MS/MS system.

LC-MS/MS analysis and peptide/protein identification

Online LC-MS was performed using a Dionex UltiMate 3000 RSLCnano System coupled to a Q-Exactive-HF mass spectrometer (Thermo Scientific). IP samples were trapped on a C18 guard-desalting column (Acclaim PepMap 100, 75 μm x 2 cm, nanoViper,

C18, 5 μm, 100 Å), and separated on a 50 cm long C18 column (Easy spray PepMap RSLC, C18, 2 μm, 100 Å, 75 μm x 50 cm). The nano capillary solvent A was 95% water, 5% DMSO, 0.1% formic acid; and solvent B was 5% water, 5% DMSO, 95% acetonitrile, 0.1% formic acid. At a constant flow of 0.25 μL min^{-1}, the curved gradient went from 2% B up to 40% B in 240 min, followed by a steep increase to 100% B in 5 min.

FTMS master scans with 70,000 resolution (and mass range 300-1700 m/z) were followed by data-dependent MS/MS (35,000 resolution) on the top 5 ions using higher energy collision dissociation (HCD) at 30%–40% normalized collision energy. Precursors were isolated with a 2 m/z window. Automatic gain control (AGC) targets were $1e^6$ for MS1 and $1e^5$ for MS2. Maximum injection times were 100 ms for MS1 and 150-200 ms for MS2. The entire duty cycle lasted ~2.5 s. Dynamic exclusion was used with 60 s duration. Precursors with unassigned charge state or charge state 1 was excluded and an underfill ratio of 1% was used.

The proteins detected in those samples were input to online Enrichr (Ma'ayan Laboratory, Computational systems biology) for Panther pathway analyses (Chen et al., 2013; Kuleshov et al., 2016).

QUANTIFICATION AND STATISTICAL ANALYSIS

Graphs and statistical analysis were performed using GraphPad Prism software. Statistical significance in Figures 2C, 2E, 2G, 2I, 3C, 4 E, 4F, 6 F, 6G, 7 C, 7E, S3B–S3D, S6D, and S6E were determined by unpaired two-tailed Student's t test. Data in Figure 3B was analyzed by linear regression. Tumor incidence/survival curve (Figures 7F and 7G) were compared by Log-rank (Mantel-Cox) test. The numbers of biological replicate samples and *P value*s (n.s., not significant, *$p < 0.05$, **$p < 0.01$, *** $p < 0.001$) are provided in individual figures. $p < 0.05$ were considered statistically significant.

Cell Reports, Volume *36*

Supplemental information

The Amot/integrin protein complex transmits mechanical forces required for vascular expansion

Yuanyuan Zhang, Yumeng Zhang, Sumako Kameishi, Giuseppina Barutello, Yujuan Zheng, Nicholas P. Tobin, John Nicosia, Katharina Hennig, David Kung-Chun Chiu, Martial Balland, Thomas H. Barker, Federica Cavallo, and Lars Holmgren

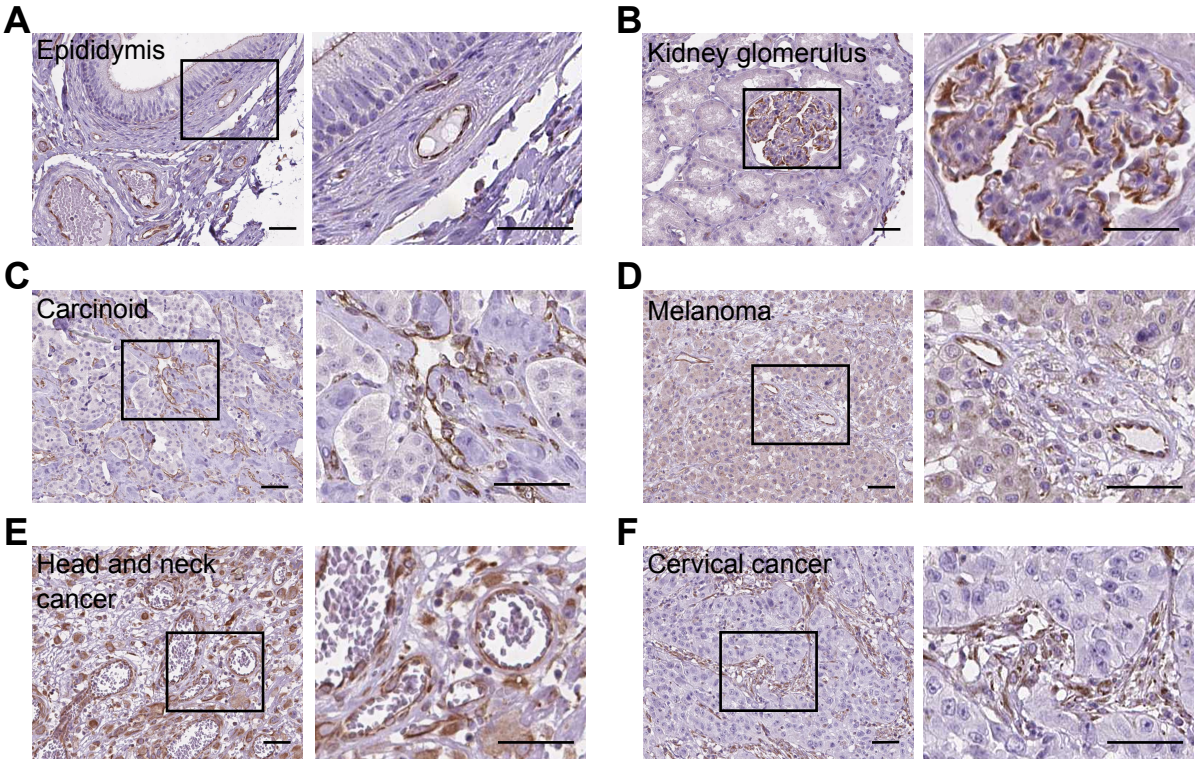

Figure S1. Localization of Amot in blood vessels of human tissues. Related to Figure 1.

(A-F) Representative IHC images of Amot expression (in brown) is shown in section of epididymis (A), kidney glomerulus (B) and pathological tissue sections, including carcinoid (C), melanoma (D), head and neck cancer (E) and cervical cancer (F). Magnification of the boxed area at left panels is shown on the right side. Scale bars, 50 μm.

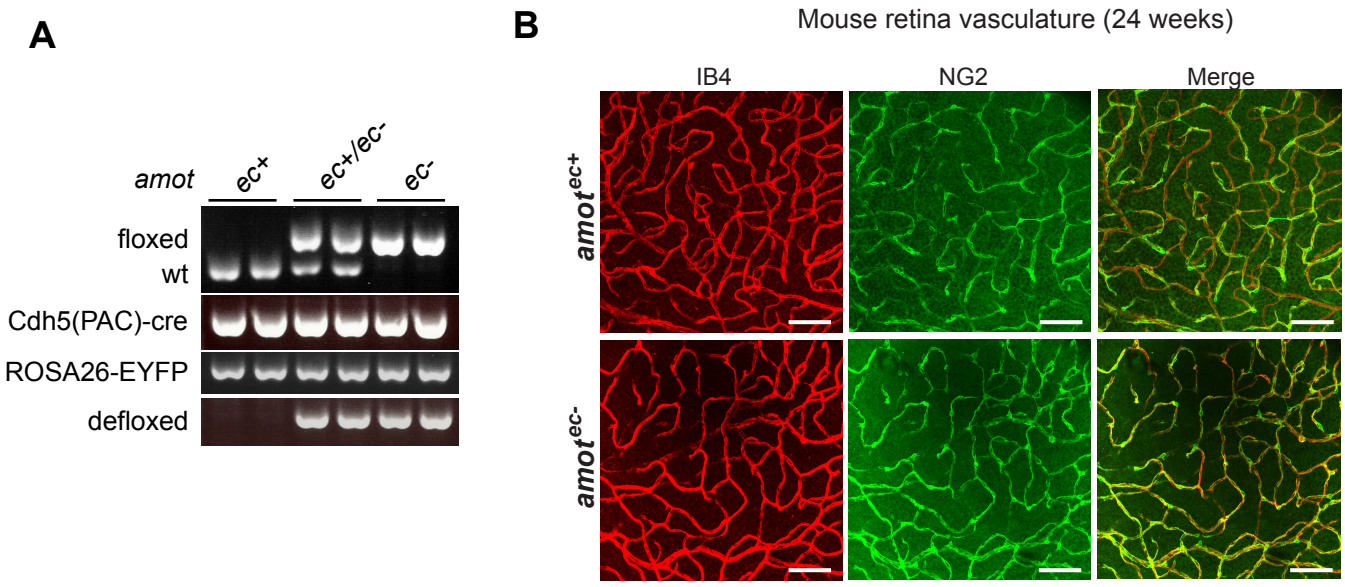

Figure S2. Vasculature in adult retina was not affected in *amot*$^{ec-}$ mice. Related to Figure 2.

(A) Genotyping of *amot*$^{ec+}$, *amot*$^{ec+/ec-}$ and *amot*$^{ec-}$ mice. DNA was isolated from ear/tail tissue. Two genomic DNA samples from each group were randomly chosen for PCR analysis for *amot*-floxed, Cdh5(PAC)-CreERT2, ROSA26-EYFP reporter and *amot*-defloxed. As the *amot* gene is localized on the X chromosome the male genotype can be *amot*$^{ec+}$ or *amot*$^{ec-}$, while the females can be *amot*$^{ec+/ec+}$, *amot*$^{ec+/ec-}$ or *amot*$^{ec-/ec-}$. However, in this study, *amot*$^{ec+/ec-}$ was not included, and therefore we used *amot*$^{ec+}$ and *amot*$^{ec-}$ to represent wild-type and *amot* knockout mice, respectively. Primers are listed in **Key Resources Table**. (B) Retinal fluorescent images with blood vessel network (IB4, in red) and mural cell staining (NG2, in green) in *amot*$^{ec+}$ and *amot*$^{ec-}$ retinas of adult age (24 weeks, n=6 for each group. The capillaries from intermediate and deep layers were merged. Scale bars, 100 μm.

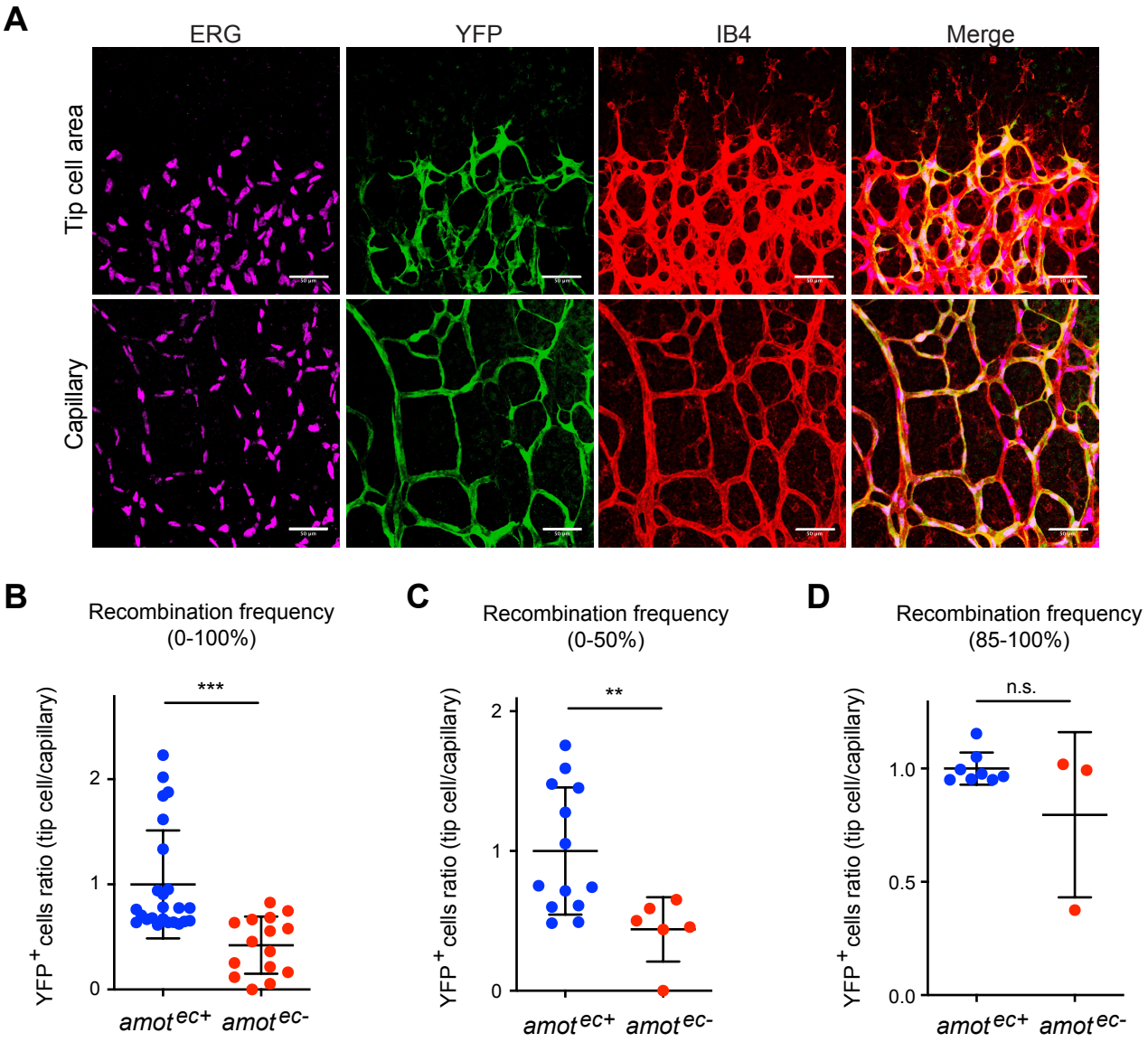

Figure S3. Amot enables ECs to take tip cell position. Related to Figure 3.

(A) Vasculature in tip cell position and capillary area was visualized by IB4 staining (in red) in *amot*$^{ec+}$ retinas of P6. ERG (in magenta) as specific nuclear EC marker was stained to facilitate the quantification of ROSA26-EYFP positive (YFP^{+}) EC cells (in green). Scale bars, 50 μm. (B-D) Quantification of YFP^{+} EC ratio between tip cell position and capillary in *amot*$^{ec+}$ and *amot*$^{ec-}$ retinas. All *amot*$^{ec+}$ retinas (n=25) and *amot*$^{ec-}$ retinas (n=15) were analyzed for statistical difference in (B). Retinas with recombination frequencies of 0-50% at capillaries (*amot*$^{ec+}$ n=13; *amot*$^{ec-}$ n=6) were analyzed in (C), and high recombination group (85-100%) was compared in (D) (*amot*$^{ec+}$ n=8; *amot*$^{ec-}$ n=3). For each sample, at least three representative images were taken from tip cell and capillary area, respectively. *n.s*, not significant, $^{**}P < 0.01$ and $^{***}P < 0.001$.

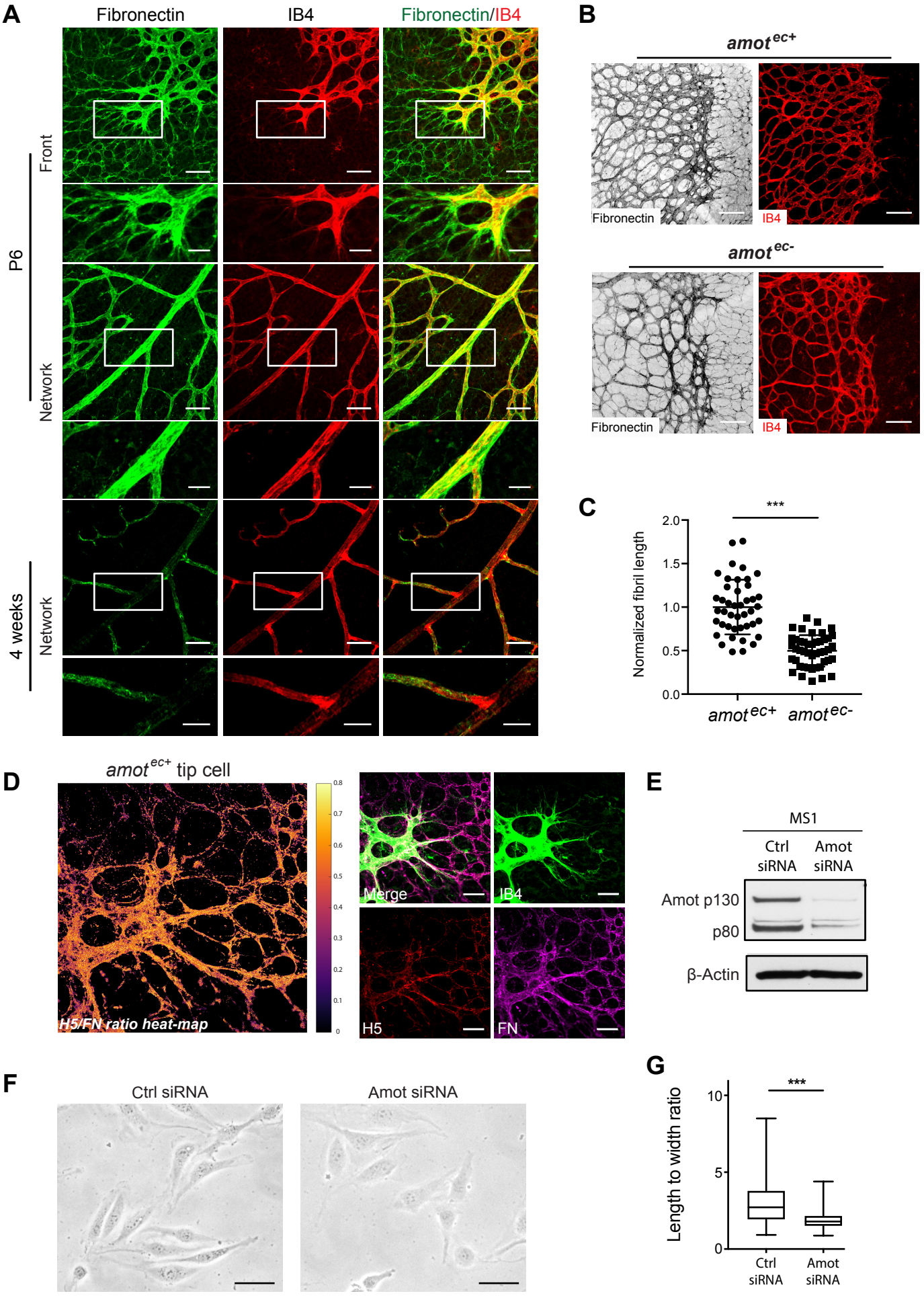
A
Fibronectin
IB4
Fibronectin/IB4
P6
Front
Network
4 weeks
Network
B
amot ec+
Fibronectin
IB4
amot ec-
Fibronectin
IB4
C
***
Normalized fibril length
2.0
1.5
1.0
0.5
0.0
amot ec+
amot ec-
D
amot ec+ tip cell
H5/FN ratio heat-map
0.8
0.7
0.6
0.5
0.4
0.3
0.2
0.1
0
Merge
IB4
H5
FN
E
MS1
Ctrl siRNA
Amot siRNA
Amot p130
p80
β-Actin
F
Ctrl siRNA
Amot siRNA
G
***
Length to width ratio
10
5
0
Ctrl siRNA
Amot siRNA

Figure S4. Amot relays force between matrix and EC. Related to Figure 4.

(A) Fn (in green) in wild-type retinas from P6 and adult age (4 week) was visualized by IF staining. Blood vessels were stained by IB4 (in red). Images of vascular fronts and capillaries at P6 are positioned in the upper and middle panels, respectively, while images of superficial vasculature from adult retina were placed at the bottom panel. White boxes indicate areas shown in higher magnification. (B) Fn expression pattern in $amot^{ec+}$ and $amot^{ec-}$ retinas at P6. Retinas were whole-mount stained with Fn (in grayscale) and IB4 (in red). (C) Dot plot illustrating the quantification of the Fn fibril length in both in $amot^{ec+}$ (n=43 from 3 mice) and $amot^{ec-}$ (n=45 from 3 mice) retinas. The average of the length in the wild-type retinas was normalized to 1. (D) Heatmap showing the ratio of H5/Fn fluorescent intensity at $amot^{ec+}$ retina at P6. Retinal fluorescent images were stained with H5-myc (in red) showing strained Fn distribution, pan-Fn (in magenta) and IB4 (in green). (E) WB verification of Amot siRNA depletion in MS1 cells. (F) Bright field images showing the cellular shape of MS1 cells transfected by control or Amot siRNA. (G) Quantification of ratio of cellular length/width in the box blot. Control group: n=103; Amot knockdown group: n=98. $^{***}P < 0.001$. Scale bars, (A) 50 μm, and 25 μm in the magnified images, (B) 100 μm, (D) 50 μm, (F) 25 μm.

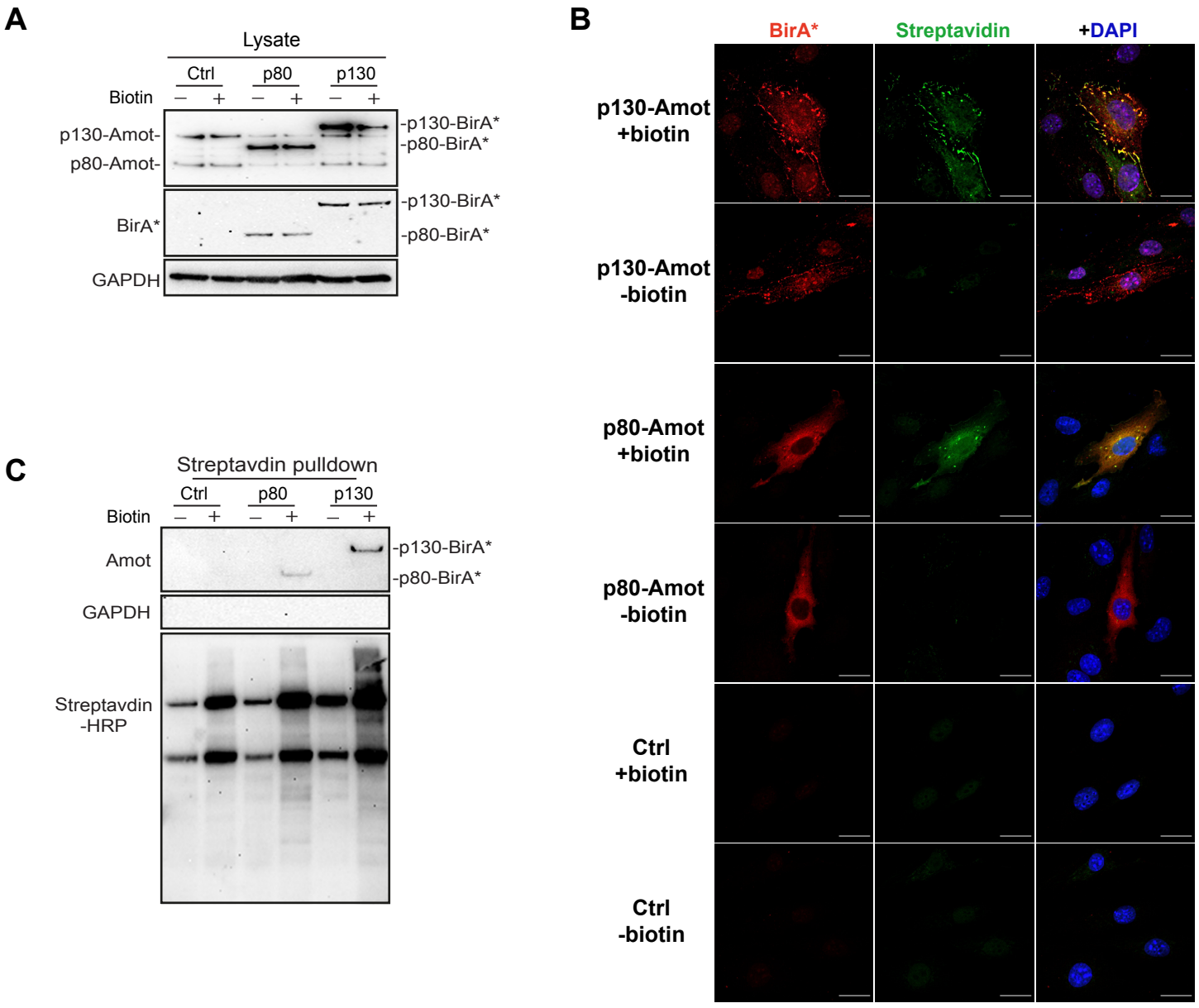

Figure S5. Amot is a novel component of the integrin adhesome. Related to Figure 5.

(A-C) WB analysis BioID-fusion protein expression in transfected MS1 cells, including empty vector, p80-Amot BioID or p130-Amot BioID. Biotin ligase BirA is activated by 16-hour incubation of of 20nM biotin. (B) IF staining of BirA and Streptavidin in transfected MS1 cells. Scale bar, 20 μm. (C) WB analysis of IP of using streptavidin sepharose, probed with antibodies against Amot and streptavidin-HRP. GAPDH was included as a non-binding negative control.

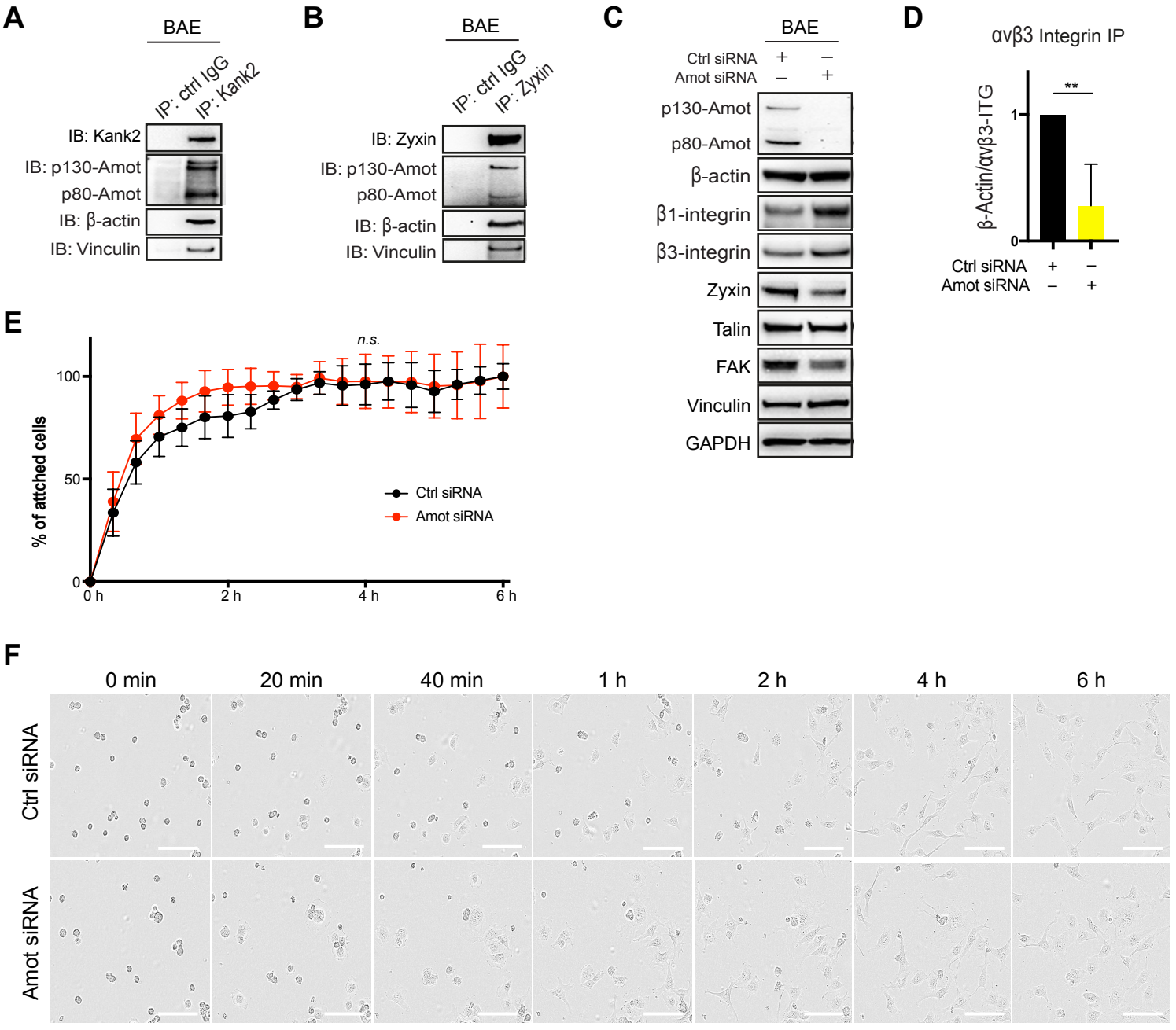
A
BAE
IP: ctrl IgG
IP: Kank2
IB: Kank2
IB: p130-Amot
p80-Amot
IB: β-actin
IB: Vinculin
B
BAE
IP: ctrl IgG
IP: Zyxin
IB: Zyxin
IB: p130-Amot
p80-Amot
IB: β-actin
IB: Vinculin
C
BAE
Ctrl siRNA + –
Amot siRNA – +
p130-Amot
p80-Amot
β-actin
β1-integrin
β3-integrin
Zyxin
Talin
FAK
Vinculin
GAPDH
D
αvβ3 Integrin IP
β-Actin/αvβ3-ITG
**
1
0
Ctrl siRNA + –
Amot siRNA – +
E
n.s.
% of attched cells
100
50
0
0 h
2 h
4 h
6 h
Ctrl siRNA
Amot siRNA
F
0 min
20 min
40 min
1 h
2 h
4 h
6 h
Ctrl siRNA
Amot siRNA

Figure S6. Amot promotes actin filament formation at focal adhesions. Related to Figure 6.

(A-B) WB verification Amot and Kank2 (A) and Zyxin (B) interaction by Co-IP in sub-confluent BAE cells (40%). Rabbit IgG was included as a negative control. (C) Steady-state levels of expression of focal adhesion related molecules in control or Amot siRNA depleted cells as analyzed by WB. The lysates were harvested from the BAE cells transfected by control or Amot siRNA. (D) Quantification of the intensity of actin using ImageJ in αvβ3-integrin IP samples. The quantities of β-actin were normalized to expression of αvβ3-integrin. All data above were collected from at least three independent experiments. $^{**}P < 0.01$. (E) Line graph depicting the percentage (%) of attached BAE cells after plating as evaluated by IncuCyte ZOOM™ live imaging system. Same number of BAE cells treated by control or Amot siRNA were plated separately on 6-well plate and the images were taken every 20 mins from beginning to 6 hours. Data are presented as mean ± SEM. Four independent experiments have been performed and the representative bright field images at time points were shown in (F). Scale bars: 50 μm. *n.s*, not significant.

Table S1. MS analysis (Amot IP in BAE cells). Related to Figure 5

Table S2. Panther pathway analysis of Amot IP-MS data in BAE cells. Related to Figure 5

Term	Overlap	P-value	Adjusted P-value	Log10 adjusted P-vaue	Genes
Cytoskeletal regulation by Rho GTPase_Homo sapiens_P00016	9/70	7,948E-07	2,54336E-05	4,594592163	VASP;ACTA1;TUBB6;TUBB2A;MYH14;MYH9;TUBB4B;MYH10;ACTB
Integrin signalling pathway_Homo sapiens_P00034	11/156	1,90226E-05	0,000304361	3,516610998	VASP;ITGB1;ITGA3;ITGA2;ITGA1;FN1;FLNA;ITGAV;LAMC1;ITGA5;ACTB
Parkinson disease_Homo sapiens_P00049	7/81	0,000181887	0,001940124	2,712170422	HSPA9;HSPA8;HSPA5;YWHAQ;YWHAZ;YWHAH;HSPA1A
Nicotinic acetylcholine receptor signaling pathway_Homo sapiens_P00044	6/68	0,000471379	0,003771034	2,423539552	ACTA1;MYO1E;MYH14;MYH9;MYH10;ACTB
Apoptosis signaling pathway_Homo sapiens_P00006	5/102	0,01693816	0,094896565	1,022749509	HSPA8;BAG4;HSPA5;HSPA1A;NFKB2
Inflammation mediated by chemokine and cytokine signaling pathway_Homo sapiens_P00031	7/188	0,020758624	0,094896565	1,022749509	ITGB1;ACTA1;MYH14;MYH9;MYH10;ACTB;NFKB2
Blood coagulation_Homo sapiens_P00011	3/38	0,01782967	0,094896565	1,022749509	SERPINC1;SERPINE1;F2
CCKR signaling map ST_Homo sapiens_P06959	6/165	0,034421897	0,126208838	0,898910233	ITGB1;SERPINE1;RPS6;HSPB1;ITGAV;CLU
Huntington disease_Homo sapiens_P00029	5/124	0,035496236	0,126208838	0,898910233	ACTA1;TUBB6;TUBB2A;TUBB4B;ACTB
Dopamine receptor mediated signaling pathway_Homo sapiens_P05912	2/52	0,175863725	0,401974228	0,39580179	PPP1CC;FLNA
EGF receptor signaling pathway_Homo sapiens_P00018	3/109	0,213337208	0,426674416	0,369903397	YWHAQ;YWHAZ;YWHAH
p53 pathway_Homo sapiens_P00059	2/71	0,27780961	0,493883752	0,306375262	SERPINE1;THBS1
FGF signaling pathway_Homo sapiens_P00021	2/99	0,425218704	0,566958271	0,246448904	YWHAQ;YWHAZ
Alzheimer disease-presenilin pathway_Homo sapiens_P00004	2/99	0,425218704	0,566958271	0,246448904	ACTA1;ACTB
VEGF signaling pathway_Homo sapiens_P00056	1/54	0,54854247	0,649236528	0,187597053	HSPB1
Cadherin signaling pathway_Homo sapiens_P00012	2/150	0,646221165	0,702837194	0,153145264	ACTA1;ACTB
T cell activation_Homo sapiens_P00053	1/73	0,65890987	0,702837194	0,153145264	NFKB2
Angiogenesis_Homo sapiens_P00005	1/142	0,877044778	0,905336545	0,043189949	HSPB1
Wnt signaling pathway_Homo sapiens_P00057	1/278	0,983715036	0,983715036	0,00713069	ACTA1

299 proteins listed in Table S1
Top 20 enrtiched pathways
Statistical information
http://amp.pharm.mssm.edu/Enrichr

Table S3. MS anlysis (p130-Amot BioID). Related to Figure 5

Original readout

Protein	Ctrl -Biotin		p80 -Biotin		p130 -Biotin		Ctrl +Biotin		p80 +Biotin		p130 +Biotin		Log10 (fold change)
Amot	0,000E0	0,000E0	0,000E0	0,000E0	0,000E0	0,000E0	0,000E0	0,000E0	9,416E7	4,498E7	4,722E8	3,525E8	8,61530
Tjp1	0,000E0	0,000E0	0,000E0	0,000E0	0,000E0	0,000E0	0,000E0	0,000E0	1,069E8	7,358E7	1,346E9	1,572E9	9,16402
Afdn	0,000E0	0,000E0	0,000E0	0,000E0	0,000E0	0,000E0	0,000E0	0,000E0	1,803E7	2,910E7	2,590E8	3,108E8	8,45472
Jcad	0,000E0	0,000E0	0,000E0	0,000E0	0,000E0	0,000E0	0,000E0	0,000E0	1,540E7	1,345E7	1,475E8	2,498E8	8,29810
Shroom4	0,000E0	0,000E0	0,000E0	0,000E0	0,000E0	0,000E0	0,000E0	0,000E0	7,815E7	4,982E7	1,518E8	1,881E8	8,23040
Lpp	0,000E0	0,000E0	0,000E0	0,000E0	0,000E0	0,000E0	0,000E0	0,000E0	5,242E6	6,804E6	2,746E7	1,037E8	7,81665
Tjp2	0,000E0	0,000E0	0,000E0	0,000E0	0,000E0	0,000E0	0,000E0	0,000E0	6,473E6	4,853E6	3,019E7	9,357E7	7,79154
Magi1	0,000E0	0,000E0	0,000E0	0,000E0	0,000E0	0,000E0	0,000E0	0,000E0	0,000E0	0,000E0	5,558E7	4,671E7	7,70881
Shroom2	0,000E0	0,000E0	0,000E0	0,000E0	0,000E0	0,000E0	0,000E0	0,000E0	7,310E6	1,320E7	5,022E7	3,776E7	7,64336
Cgnl1	0,000E0	0,000E0	0,000E0	0,000E0	0,000E0	0,000E0	0,000E0	0,000E0	5,471E6	1,290E6	4,686E7	2,561E7	7,55910
Synpo	0,000E0	0,000E0	0,000E0	0,000E0	0,000E0	0,000E0	0,000E0	0,000E0	0,000E0	0,000E0	3,450E7	3,592E7	7,54668
Amotl1	0,000E0	0,000E0	0,000E0	0,000E0	0,000E0	0,000E0	0,000E0	0,000E0	3,914E7	3,990E7	1,654E7	1,887E7	7,24812
Mpdz	0,000E0	0,000E0	0,000E0	0,000E0	0,000E0	0,000E0	0,000E0	0,000E0	1,008E7	1,129E7	1,336E7	1,857E7	7,20313
Yap1	0,000E0	0,000E0	0,000E0	0,000E0	0,000E0	0,000E0	0,000E0	0,000E0	6,568E6	6,665E6	9,906E6	2,096E7	7,18846
Crkl	0,000E0	0,000E0	0,000E0	0,000E0	0,000E0	0,000E0	0,000E0	0,000E0	0,000E0	7,002E6	2,910E7	8,951E5	7,17608
Sipa1	0,000E0	0,000E0	0,000E0	0,000E0	0,000E0	0,000E0	0,000E0	0,000E0	2,996E6	0,000E0	1,372E7	1,494E7	7,15622
Tp53bp2	0,000E0	0,000E0	0,000E0	0,000E0	0,000E0	0,000E0	0,000E0	0,000E0	2,075E7	6,426E6	1,561E7	1,301E7	7,15564
Ly6c1	0,000E0	0,000E0	0,000E0	0,000E0	0,000E0	0,000E0	0,000E0	0,000E0	3,000E7	1,403E7	5,471E6	2,284E7	7,15088
Pdlim7	0,000E0	0,000E0	0,000E0	0,000E0	0,000E0	0,000E0	0,000E0	0,000E0	0,000E0	0,000E0	8,944E6	1,795E7	7,12867
Pdlim5	0,000E0	0,000E0	0,000E0	0,000E0	0,000E0	0,000E0	0,000E0	0,000E0	0,000E0	0,000E0	1,696E7	7,680E6	7,09062
Zyx	0,000E0	0,000E0	0,000E0	0,000E0	0,000E0	0,000E0	0,000E0	0,000E0	0,000E0	0,000E0	7,413E6	1,525E7	7,05431
Cttn	0,000E0	0,000E0	0,000E0	0,000E0	0,000E0	0,000E0	0,000E0	0,000E0	9,298E6	7,480E6	1,827E7	3,848E6	7,04379
Kif14	0,000E0	0,000E0	0,000E0	0,000E0	0,000E0	0,000E0	0,000E0	0,000E0	0,000E0	1,475E6	7,520E6	1,352E7	7,02200
Rassf8	0,000E0	0,000E0	0,000E0	0,000E0	0,000E0	0,000E0	0,000E0	0,000E0	4,587E6	0,000E0	1,132E7	6,952E6	6,96076
Dlg5	0,000E0	0,000E0	0,000E0	0,000E0	0,000E0	0,000E0	0,000E0	0,000E0	3,285E6	1,196E6	3,201E6	1,312E7	6,91171
Ctnnd1	0,000E0	0,000E0	0,000E0	0,000E0	0,000E0	0,000E0	0,000E0	0,000E0	0,000E0	8,505E5	9,953E6	5,037E6	6,87478
Flna	0,000E0	0,000E0	0,000E0	0,000E0	0,000E0	0,000E0	0,000E0	0,000E0	3,235E6	3,604E6	8,537E6	5,856E6	6,85713
Sorbs2	0,000E0	0,000E0	0,000E0	0,000E0	0,000E0	0,000E0	0,000E0	0,000E0	0,000E0	0,000E0	5,034E6	8,404E6	6,82731
Gars	0,000E0	0,000E0	0,000E0	0,000E0	0,000E0	0,000E0	0,000E0	0,000E0	4,338E6	3,546E6	8,423E6	4,998E6	6,82675
Fbl	0,000E0	0,000E0	0,000E0	0,000E0	0,000E0	0,000E0	0,000E0	0,000E0	8,468E6	2,231E6	3,599E6	9,606E6	6,81972
Swap70	0,000E0	0,000E0	0,000E0	0,000E0	0,000E0	0,000E0	0,000E0	0,000E0	9,452E6	3,962E6	6,543E6	5,429E6	6,77717
Ccdc85c	0,000E0	0,000E0	0,000E0	0,000E0	0,000E0	0,000E0	0,000E0	0,000E0	0,000E0	0,000E0	6,466E6	4,970E6	6,75722
Flnb	0,000E0	0,000E0	0,000E0	0,000E0	0,000E0	0,000E0	0,000E0	0,000E0	5,100E6	4,609E6	6,327E6	4,587E6	6,73696
Copa	0,000E0	0,000E0	0,000E0	0,000E0	0,000E0	0,000E0	0,000E0	0,000E0	2,440E6	2,543E6	4,164E6	5,347E6	6,67721
Tln1	0,000E0	0,000E0	0,000E0	0,000E0	0,000E0	0,000E0	0,000E0	0,000E0	3,006E6	1,186E6	4,176E6	5,283E6	6,67482
Baz1b	0,000E0	0,000E0	0,000E0	0,000E0	0,000E0	0,000E0	0,000E0	0,000E0	0,000E0	0,000E0	3,559E6	5,449E6	6,65356
Cse1l	0,000E0	0,000E0	0,000E0	0,000E0	0,000E0	0,000E0	0,000E0	0,000E0	2,415E6	1,656E6	5,505E6	3,454E6	6,65123
Micall2	0,000E0	0,000E0	0,000E0	0,000E0	0,000E0	0,000E0	0,000E0	0,000E0	0,000E0	0,000E0	5,400E6	2,932E6	6,61970
Crk	0,000E0	0,000E0	0,000E0	0,000E0	0,000E0	0,000E0	0,000E0	0,000E0	1,353E6	3,142E6	7,801E5	7,383E6	6,61083
Actr2	0,000E0	0,000E0	0,000E0	0,000E0	0,000E0	0,000E0	0,000E0	0,000E0	1,058E6	4,738E6	2,992E6	5,076E6	6,60573
Wwc2	0,000E0	0,000E0	0,000E0	0,000E0	0,000E0	0,000E0	0,000E0	0,000E0	1,941E6	0,000E0	5,451E6	2,528E6	6,60089
Dvl2	0,000E0	0,000E0	0,000E0	0,000E0	0,000E0	0,000E0	0,000E0	0,000E0	3,992E6	0,000E0	2,747E6	5,142E6	6,59601
Nckap1	0,000E0	0,000E0	0,000E0	0,000E0	0,000E0	0,000E0	0,000E0	0,000E0	1,508E6	5,671E5	2,553E6	5,163E6	6,58636
Pard3	0,000E0	0,000E0	0,000E0	0,000E0	0,000E0	0,000E0	0,000E0	0,000E0	0,000E0	0,000E0	2,118E6	5,223E6	6,56469
Ddx39a	0,000E0	0,000E0	0,000E0	0,000E0	0,000E0	0,000E0	0,000E0	0,000E0	1,205E7	3,246E6	4,607E6	2,665E6	6,56064
Atp1a1	0,000E0	0,000E0	0,000E0	0,000E0	0,000E0	0,000E0	0,000E0	0,000E0	7,579E5	0,000E0	2,867E6	4,078E6	6,54066
Akap2	0,000E0	0,000E0	0,000E0	0,000E0	0,000E0	0,000E0	0,000E0	0,000E0	2,148E6	5,235E5	1,704E6	5,055E6	6,52888
Rps24	0,000E0	0,000E0	0,000E0	0,000E0	0,000E0	0,000E0	0,000E0	0,000E0	0,000E0	7,616E6	4,814E6	1,817E6	6,52056
Tpm3	0,000E0	0,000E0	0,000E0	0,000E0	0,000E0	0,000E0	0,000E0	0,000E0	0,000E0	2,739E6	3,329E6	2,736E6	6,48180
Fxr2	0,000E0	0,000E0	0,000E0	0,000E0	0,000E0	0,000E0	0,000E0	0,000E0	0,000E0	0,000E0	9,801E5	4,737E6	6,45618
Kank2	0,000E0	0,000E0	0,000E0	0,000E0	0,000E0	0,000E0	0,000E0	0,000E0	7,248E5	0,000E0	3,607E6	1,650E6	6,41968
Parp1	0,000E0	0,000E0	0,000E0	0,000E0	0,000E0	0,000E0	0,000E0	0,000E0	0,000E0	0,000E0	1,131E6	4,096E6	6,41724
Dync1h1	0,000E0	0,000E0	0,000E0	0,000E0	0,000E0	0,000E0	0,000E0	0,000E0	3,440E6	1,999E6	3,107E6	1,590E6	6,37080
Nf2	0,000E0	0,000E0	0,000E0	0,000E0	0,000E0	0,000E0	0,000E0	0,000E0	4,492E6	1,335E7	1,142E5	4,509E6	6,36396
Rpn1	0,000E0	0,000E0	0,000E0	0,000E0	0,000E0	0,000E0	0,000E0	0,000E0	0,000E0	0,000E0	1,285E6	3,189E6	6,34960
Nars	0,000E0	0,000E0	0,000E0	0,000E0	0,000E0	0,000E0	0,000E0	0,000E0	0,000E0	2,485E6	2,322E6	2,115E6	6,34604
Chtop	0,000E0	0,000E0	0,000E0	0,000E0	0,000E0	0,000E0	0,000E0	0,000E0	0,000E0	0,000E0	1,630E6	2,701E6	6,33548
Ranbp2	0,000E0	0,000E0	0,000E0	0,000E0	0,000E0	0,000E0	0,000E0	0,000E0	3,113E6	2,448E6	7,706E5	3,425E6	6,32178
Magi3	0,000E0	0,000E0	0,000E0	0,000E0	0,000E0	0,000E0	0,000E0	0,000E0	0,000E0	0,000E0	2,208E6	1,974E6	6,32034
Sptbn1	0,000E0	0,000E0	0,000E0	0,000E0	0,000E0	0,000E0	0,000E0	0,000E0	2,701E6	2,132E6	2,558E6	1,430E6	6,29966
Snd1	0,000E0	0,000E0	0,000E0	0,000E0	0,000E0	0,000E0	0,000E0	0,000E0	4,075E6	1,826E6	2,587E6	1,238E6	6,28167
Eif3a	0,000E0	0,000E0	0,000E0	0,000E0	0,000E0	0,000E0	0,000E0	0,000E0	0,000E0	0,000E0	6,156E5	2,730E6	6,22341
Tpx2	0,000E0	0,000E0	0,000E0	0,000E0	0,000E0	0,000E0	0,000E0	0,000E0	0,000E0	0,000E0	2,223E6	1,029E6	6,21112
Wdr1	0,000E0	0,000E0	0,000E0	0,000E0	0,000E0	0,000E0	0,000E0	0,000E0	2,509E6	3,096E6	7,852E5	2,430E6	6,20614
Asns	0,000E0	0,000E0	0,000E0	0,000E0	0,000E0	0,000E0	0,000E0	0,000E0	0,000E0	0,000E0	1,140E6	2,061E6	6,20417
Nat10	0,000E0	0,000E0	0,000E0	0,000E0	0,000E0	0,000E0	0,000E0	0,000E0	0,000E0	0,000E0	8,053E5	2,359E6	6,19928
Cyfip2	0,000E0	0,000E0	0,000E0	0,000E0	0,000E0	0,000E0	0,000E0	0,000E0	8,012E5	1,143E6	2,029E5	2,587E6	6,14461
Flnc	0,000E0	0,000E0	0,000E0	0,000E0	0,000E0	0,000E0	0,000E0	0,000E0	1,144E6	0,000E0	2,339E6	1,631E5	6,09726
Fau	0,000E0	0,000E0	0,000E0	0,000E0	0,000E0	0,000E0	0,000E0	0,000E0	0,000E0	0,000E0	8,549E5	1,102E6	5,99049
Pdcd11	0,000E0	0,000E0	0,000E0	0,000E0	0,000E0	0,000E0	0,000E0	0,000E0	0,000E0	0,000E0	6,227E5	8,145E5	5,85649
Prpf8	0,000E0	0,000E0	0,000E0	0,000E0	0,000E0	0,000E0	0,000E0	0,000E0	0,000E0	0,000E0	6,448E5	7,501E5	5,84351
Actr3	0,000E0	0,000E0	0,000E0	0,000E0	0,000E0	0,000E0	0,000E0	0,000E0	0,000E0	0,000E0	1,175E5	4,395E5	5,44483
Eif3l	0,000E0	0,000E0	0,000E0	0,000E0	0,000E0	4,616E4	0,000E0	0,000E0	1,646E6	2,378E6	1,785E6	2,744E6	2,59380
Dynll1	0,000E0	0,000E0	0,000E0	7,622E4	0,000E0	0,000E0	0,000E0	0,000E0	4,357E6	4,878E6	3,801E6	2,563E6	2,52371
Cav1	0,000E0	0,000E0	0,000E0	0,000E0	1,878E6	0,000E0	0,000E0	0,000E0	9,938E6	9,421E6	2,253E7	1,353E7	1,88524
Nedd4	0,000E0	0,000E0	0,000E0	0,000E0	0,000E0	3,602E5	1,190E6	0,000E0	2,292E6	0,000E0	2,632E6	1,391E7	1,63031
Atp2a2	0,000E0	0,000E0	0,000E0	0,000E0	0,000E0	7,218E5	0,000E0	0,000E0	2,196E6	5,478E5	3,190E6	4,167E6	1,61036
H2afz	4,405E5	2,472E7	1,692E7	8,344E5	3,858E7	7,069E6	5,100E7	0,000E0	2,122E6	1,434E7	1,406E8	1,178E9	1,57735
Smc4	0,000E0	0,000E0	0,000E0	0,000E0	0,000E0	1,864E6	0,000E0	0,000E0	1,353E6	4,003E6	8,556E6	8,100E6	1,55315
Abcf2	0,000E0	0,000E0	0,000E0	0,000E0	0,000E0	4,524E5	0,000E0	0,000E0	3,616E6	3,094E6	1,513E6	2,101E6	1,50446
Ywhab	1,928E6	0,000E0	0,000E0	0,000E0	0,000E0	0,000E0	0,000E0	0,000E0	5,409E6	1,717E7	1,213E7	3,149E6	1,50101
Rrbp1	0,000E0	0,000E0	0,000E0	7,381E5	0,000E0	1,064E6	0,000E0	0,000E0	2,696E6	1,716E6	6,773E6	7,426E6	1,49858
Slc25a13	0,000E0	0,000E0	0,000E0	0,000E0	0,000E0	0,000E0	5,181E5	0,000E0	0,000E0	0,000E0	1,546E6	2,150E6	1,45533
Psat1	0,000E0	0,000E0	0,000E0	0,000E0	0,000E0	0,000E0	9,430E5	0,000E0	3,756E6	2,909E6	4,454E6	1,801E6	1,42377
Ywhae	1,928E6	0,000E0	0,000E0	0,000E0	0,000E0	0,000E0	0,000E0	0,000E0	4,989E6	2,879E6	8,585E6	3,990E6	1,41641
Lbr	0,000E0	0,000E0	0,000E0	0,000E0	0,000E0	2,279E6	0,000E0	0,000E0	6,634E6	0,000E0	2,506E6	1,225E7	1,41319
Hist1h2ah	2,149E7	1,380E7	3,213E7	7,339E6	2,282E7	3,576E7	4,141E7	0,000E0	5,241E7	1,996E7	1,512E8	8,570E8	1,36324
Hist2h2ac	1,795E7	1,617E7	3,300E7	9,178E6	1,614E7	3,808E7	4,607E7	0,000E0	6,645E7	2,035E7	1,356E8	8,721E8	1,35842
Hnrnpf	0,000E0	0,000E0	0,000E0	0,000E0	0,000E0	2,688E6	0,000E0	0,000E0	0,000E0	0,000E0	5,478E6	9,737E6	1,35488
Actn4	1,574E6	0,000E0	0,000E0	0,000E0	0,000E0	2,131E6	1,414E6	0,000E0	5,572E6	2,355E6	1,043E7	1,846E7	1,35353
Myof	0,000E0	0,000E0	1,109E6	0,000E0	5,501E5	0,000E0	0,000E0	0,000E0	4,798E6	3,975E6	4,662E6	4,642E6	1,35098

Rpl26	0,000E0	1,318E7	0,000E0	0,000E0	0,000E0	4,210E6	0,000E0	0,000E0	1,007E7	1,790E6	5,645E7	4,020E7	1,34707
Alyref	0,000E0	0,000E0	0,000E0	0,000E0	0,000E0	1,741E6	0,000E0	0,000E0	0,000E0	0,000E0	4,263E6	5,063E6	1,33097
Mki67	0,000E0	0,000E0	0,000E0	0,000E0	0,000E0	1,615E6	0,000E0	0,000E0	0,000E0	0,000E0	2,836E6	5,557E6	1,31787
Capn2	0,000E0	0,000E0	0,000E0	0,000E0	0,000E0	2,631E6	0,000E0	0,000E0	0,000E0	0,000E0	5,836E6	7,679E6	1,31284
Actn1	1,574E6	0,000E0	0,000E0	0,000E0	0,000E0	3,258E6	1,458E6	0,000E0	3,011E6	3,145E6	1,333E7	1,557E7	1,26429
Kcnk3	0,000E0	0,000E0	0,000E0	0,000E0	1,391E7	0,000E0	0,000E0	0,000E0	9,993E6	0,000E0	2,780E7	3,331E7	1,24497
Mcm5	0,000E0	0,000E0	0,000E0	7,741E5	2,409E6	0,000E0	2,578E6	0,000E0	5,950E6	8,675E6	1,395E7	1,117E7	1,24160
Lrpprc	0,000E0	0,000E0	0,000E0	0,000E0	0,000E0	0,000E0	2,066E6	0,000E0	9,282E6	5,736E6	2,457E6	6,188E6	1,22366
Coro1b	0,000E0	0,000E0	0,000E0	0,000E0	0,000E0	0,000E0	5,625E6	0,000E0	3,063E7	7,908E6	6,998E6	1,569E7	1,20776
Rpl23	0,000E0	0,000E0	0,000E0	0,000E0	0,000E0	8,693E5	1,540E6	0,000E0	3,112E6	2,196E6	5,209E6	4,267E6	1,19682
Ckap4	0,000E0	0,000E0	0,000E0	8,464E5	0,000E0	0,000E0	2,791E6	0,000E0	3,229E6	5,223E6	4,849E6	9,443E6	1,19635
Nop58	0,000E0	0,000E0	0,000E0	0,000E0	0,000E0	2,994E6	0,000E0	0,000E0	2,977E6	0,000E0	3,106E6	7,870E6	1,16632
Camk2d	0,000E0	0,000E0	0,000E0	0,000E0	0,000E0	0,000E0	4,344E5	0,000E0	0,000E0	4,337E6	9,658E5	5,365E5	1,14089
Bub3	0,000E0	0,000E0	0,000E0	0,000E0	0,000E0	0,000E0	7,867E5	0,000E0	0,000E0	0,000E0	8,859E5	1,742E6	1,12582
Ddx3y	0,000E0	0,000E0	0,000E0	0,000E0	0,000E0	1,365E6	7,895E5	0,000E0	0,000E0	2,531E6	5,683E6	1,496E6	1,12479
Fasn	7,091E5	1,037E6	0,000E0	0,000E0	0,000E0	0,000E0	7,059E5	0,000E0	1,492E6	1,633E6	3,665E6	4,262E6	1,11162
Rps16	2,666E6	3,349E6	2,013E6	4,925E6	8,053E6	1,481E7	4,754E5	0,000E0	4,550E7	7,904E6	1,893E7	9,364E7	1,09372
Ddx21	5,399E5	0,000E0	3,352E6	1,319E6	0,000E0	4,019E6	1,598E6	0,000E0	6,244E6	2,921E6	1,654E7	1,620E7	1,08254
Psmd2	0,000E0	0,000E0	0,000E0	0,000E0	2,884E6	8,561E5	0,000E0	0,000E0	4,032E6	4,651E6	5,687E6	5,119E6	1,06285
Slc25a5	5,057E6	5,689E6	2,100E6	3,666E6	8,061E5	8,691E6	3,208E6	0,000E0	1,906E7	4,418E7	4,618E7	3,665E7	1,05459
Rps9	3,103E6	1,698E6	3,781E6	1,213E6	6,571E5	4,158E6	6,362E6	0,000E0	2,831E7	3,773E6	3,076E7	2,852E7	1,05332
Tars	1,512E6	0,000E0	1,206E6	0,000E0	0,000E0	0,000E0	0,000E0	0,000E0	8,958E5	1,824E6	2,140E6	5,488E6	1,05013
Rhoa	4,031E6	1,554E6	0,000E0	0,000E0	1,249E6	2,195E6	0,000E0	0,000E0	1,208E7	7,005E6	6,114E6	1,813E7	1,03108
Rpl5	4,192E6	0,000E0	0,000E0	0,000E0	0,000E0	2,525E6	0,000E0	0,000E0	1,489E7	8,785E6	1,103E7	5,937E6	1,00441
Ddx6	2,957E6	0,000E0	0,000E0	0,000E0	3,206E6	0,000E0	0,000E0	0,000E0	3,461E6	3,831E6	6,166E6	9,339E6	1,00270
Slc25a4	1,698E6	7,351E6	0,000E0	1,059E6	3,352E6	1,211E7	2,933E6	0,000E0	2,164E7	1,745E7	2,958E7	4,144E7	0,99845
Rps17	0,000E0	0,000E0	0,000E0	1,502E6	5,282E5	0,000E0	6,366E5	0,000E0	3,424E6	4,714E6	5,012E6	1,517E6	0,99095
Ywhaq	1,928E6	0,000E0	0,000E0	0,000E0	0,000E0	0,000E0	2,935E6	0,000E0	5,409E6	1,060E7	8,585E6	3,149E6	0,98461
Psma1	0,000E0	0,000E0	0,000E0	0,000E0	1,168E6	0,000E0	1,726E6	0,000E0	0,000E0	2,465E6	2,512E6	4,362E6	0,97780
Rab14	0,000E0	1,164E6	0,000E0	5,827E5	0,000E0	6,900E5	0,000E0	0,000E0	1,635E6	0,000E0	2,367E6	3,416E6	0,97735
Rps2	4,037E6	4,756E6	2,043E7	1,349E7	1,156E7	1,293E7	1,255E7	0,000E0	5,062E7	3,107E7	9,003E7	9,675E7	0,97162
Rpl34	2,459E6	0,000E0	5,106E6	3,934E6	1,672E6	4,212E6	3,776E6	0,000E0	6,278E6	1,986E6	6,959E6	4,244E7	0,97032
Rpl17	0,000E0	0,000E0	0,000E0	1,475E6	1,217E6	1,960E6	4,335E6	0,000E0	3,582E6	2,663E6	5,460E6	1,465E7	0,95191
Rpl21	0,000E0	0,000E0	0,000E0	0,000E0	3,820E6	5,534E6	1,080E6	0,000E0	4,707E6	3,138E6	7,443E6	1,543E7	0,94291
Top2a	0,000E0	0,000E0	0,000E0	0,000E0	2,732E5	1,504E6	8,756E5	0,000E0	1,146E6	7,606E5	2,503E6	3,208E6	0,93497
Cfl1	8,331E6	8,908E6	6,183E6	4,811E6	1,275E6	6,316E6	2,090E6	0,000E0	2,102E7	1,768E7	3,511E7	4,298E7	0,91585
Rpl12	1,655E6	0,000E0	5,570E6	2,483E6	6,977E5	1,189E6	0,000E0	0,000E0	1,069E7	1,309E7	1,455E7	8,446E6	0,89947
Psmd3	0,000E0	0,000E0	3,080E6	0,000E0	1,784E6	4,358E6	0,000E0	0,000E0	7,291E6	3,723E6	5,636E6	1,264E7	0,89906
Surf4	7,784E5	1,001E6	0,000E0	0,000E0	0,000E0	0,000E0	5,077E5	0,000E0	3,087E6	9,124E5	1,119E6	3,356E6	0,89351
Cltc	2,599E6	6,696E5	3,339E5	0,000E0	1,912E6	0,000E0	6,301E6	0,000E0	7,028E6	6,893E6	1,095E7	1,189E7	0,88837
Ehd2	0,000E0	0,000E0	0,000E0	1,265E6	6,861E5	2,061E6	0,000E0	0,000E0	4,235E6	4,057E6	3,761E6	3,388E6	0,85284
Smarca5	0,000E0	0,000E0	0,000E0	1,908E6	0,000E0	1,669E6	0,000E0	0,000E0	1,766E6	1,851E6	2,606E6	3,663E6	0,84583
Rpl7	4,098E6	1,564E7	7,494E6	1,192E7	5,326E7	3,827E7	2,016E6	0,000E0	5,020E7	2,981E7	9,677E7	1,276E8	0,83016
Rpl10a	3,559E6	2,532E6	6,550E6	1,029E7	3,247E6	1,391E7	1,069E7	0,000E0	2,009E7	7,492E6	1,821E7	6,741E7	0,82893
Plec	4,988E6	3,298E5	1,104E6	2,140E6	1,024E6	1,638E6	1,222E6	0,000E0	6,372E6	4,756E6	1,205E7	8,915E6	0,82859
Myh9	6,562E6	7,797E6	8,951E6	6,176E6	5,226E6	6,976E6	6,888E6	0,000E0	2,237E7	3,388E7	3,792E7	4,332E7	0,82541
Slc25a3	1,718E6	1,202E6	1,668E6	8,395E5	0,000E0	0,000E0	2,094E6	0,000E0	5,960E6	2,973E6	3,063E6	9,473E6	0,82390
Snu13	0,000E0	1,892E6	0,000E0	0,000E0	1,895E6	4,215E6	0,000E0	0,000E0	2,559E6	6,488E6	5,855E6	7,065E6	0,81015
Psma6	0,000E0	0,000E0	0,000E0	0,000E0	3,395E5	1,784E6	1,743E6	0,000E0	0,000E0	0,000E0	2,405E6	3,816E6	0,80858
Mybbp1a	0,000E0	1,881E6	1,460E6	1,856E6	1,890E6	2,531E6	4,522E6	0,000E0	8,674E6	2,215E6	8,164E6	1,450E7	0,80699
Ddx5	0,000E0	0,000E0	1,101E6	2,031E6	0,000E0	0,000E0	2,058E6	0,000E0	6,245E6	5,558E6	4,494E6	3,727E6	0,80178
Hspa4	0,000E0	0,000E0	6,709E5	0,000E0	4,252E5	1,505E6	0,000E0	0,000E0	2,200E6	0,000E0	2,037E6	2,081E6	0,80168
Syncrip	0,000E0	0,000E0	0,000E0	1,726E6	1,308E6	0,000E0	9,925E5	0,000E0	4,590E6	3,174E6	2,933E6	3,219E6	0,78610
Rpl19	1,875E6	1,490E6	3,039E6	0,000E0	4,382E6	0,000E0	4,284E6	0,000E0	2,795E6	0,000E0	1,401E7	8,915E6	0,78435
Ppid	4,976E5	7,812E5	0,000E0	0,000E0	0,000E0	0,000E0	1,202E6	0,000E0	2,642E6	0,000E0	1,620E6	2,069E6	0,77435
Hist1h1c	1,959E6	2,169E7	9,713E7	2,579E7	8,749E7	9,700E7	1,901E7	0,000E0	3,575E7	2,313E7	3,105E8	1,992E8	0,76522
Hspa9	0,000E0	0,000E0	0,000E0	0,000E0	6,115E5	1,276E6	1,550E6	0,000E0	0,000E0	3,673E6	3,263E6	1,736E6	0,76465
Npm1	0,000E0	0,000E0	1,345E6	1,427E6	8,242E5	0,000E0	0,000E0	0,000E0	1,956E6	4,731E6	2,006E6	3,205E6	0,76320
Top1	0,000E0	0,000E0	8,430E5	6,894E5	2,714E5	1,902E6	2,440E6	0,000E0	6,321E6	1,992E6	4,922E6	3,947E6	0,76135
Tagln2	0,000E0	5,301E6	8,567E5	3,501E6	2,500E6	0,000E0	2,132E6	0,000E0	0,000E0	3,668E6	1,170E7	8,542E6	0,75333
Rps14	1,978E6	3,422E6	5,826E6	2,875E6	5,696E6	9,422E6	6,643E6	0,000E0	1,235E7	9,600E6	1,526E7	3,533E7	0,75153
Rpl6	1,023E7	9,293E6	5,644E6	1,491E6	4,003E6	3,165E7	1,694E7	0,000E0	2,328E7	8,804E6	3,706E7	6,975E7	0,73161
Rpl35	6,557E6	0,000E0	0,000E0	0,000E0	4,319E6	9,289E6	1,635E6	0,000E0	5,176E6	0,000E0	1,332E7	1,593E7	0,72969
Rps11	6,196E6	8,758E6	1,349E7	3,804E6	1,022E7	2,167E7	6,551E6	0,000E0	1,942E7	1,516E7	5,527E7	3,781E7	0,72158
Pcbp2	1,089E6	0,000E0	0,000E0	0,000E0	1,488E6	5,035E6	4,872E6	0,000E0	4,691E6	5,634E6	6,187E6	1,021E7	0,72047
Hnrnpu	1,702E6	2,774E6	6,167E6	4,489E6	9,921E6	1,761E7	5,165E6	0,000E0	4,496E7	3,052E7	2,274E7	3,899E7	0,71284
Pgd	0,000E0	0,000E0	1,109E6	0,000E0	0,000E0	1,028E6	1,281E6	0,000E0	4,117E6	0,000E0	2,346E6	1,593E6	0,66370
Idh2	1,535E6	0,000E0	2,211E6	5,233E5	1,080E6	3,359E6	4,176E6	0,000E0	4,253E6	9,003E6	4,751E6	9,694E6	0,65170
Mccc1	1,264E8	1,349E8	1,545E8	3,101E7	1,542E8	1,770E8	3,546E8	0,000E0	5,494E8	4,866E8	5,775E8	6,873E8	0,64997
Vars	0,000E0	0,000E0	1,930E6	4,014E6	1,761E6	2,149E6	3,742E6	0,000E0	1,699E7	8,116E6	5,965E6	8,627E6	0,63276
Myh10	0,000E0	5,258E5	2,149E6	1,432E6	1,393E6	0,000E0	6,842E5	0,000E0	6,348E6	7,126E6	3,673E6	2,857E6	0,62573
Vat1	0,000E0	7,845E6	5,438E6	4,114E6	0,000E0	3,413E6	4,410E6	0,000E0	4,659E6	1,602E7	1,078E7	1,571E7	0,62348
Pc	8,736E8	5,102E8	3,777E8	3,393E8	3,723E8	9,338E8	5,199E8	2,128E5	2,870E9	2,236E9	1,639E9	2,442E9	0,61868
Eef2	6,115E6	5,515E6	5,703E6	7,519E6	7,618E6	1,310E7	9,971E6	0,000E0	1,981E7	8,755E6	2,880E7	2,684E7	0,60285
Pcca	2,006E8	1,198E8	4,871E7	1,378E8	7,757E7	2,033E8	3,560E8	0,000E0	6,097E8	5,039E8	4,315E8	6,899E8	0,59346
Eif4a1	1,100E7	3,137E7	1,636E6	6,419E6	1,410E7	2,823E7	1,247E7	0,000E0	3,655E7	1,519E7	6,124E7	4,019E7	0,58608
Taldo1	1,979E6	0,000E0	2,450E6	5,257E6	0,000E0	3,084E6	1,381E6	0,000E0	5,739E6	5,136E6	7,877E6	5,417E6	0,57497
Serpinb6	1,641E6	0,000E0	0,000E0	0,000E0	5,332E6	4,262E6	1,533E6	0,000E0	1,848E7	6,719E6	6,075E6	5,906E6	0,57441
Crip2	0,000E0	5,011E6	1,532E6	6,881E6	9,018E5	4,907E6	0,000E0	0,000E0	3,562E6	3,808E6	1,041E7	7,356E6	0,56765
Cct8	3,317E6	2,436E6	7,735E5	3,434E5	2,249E6	3,819E6	4,811E6	0,000E0	9,072E6	1,179E7	7,018E6	8,294E6	0,53790
Esd	6,142E7	2,451E7	4,511E7	1,713E7	3,408E7	9,679E7	3,175E7	0,000E0	1,198E8	4,140E7	1,155E8	1,427E8	0,52151
Fkbp1a	5,914E6	6,765E6	5,150E6	2,507E6	6,994E6	2,373E6	1,108E6	0,000E0	8,598E6	6,499E6	7,282E6	1,647E7	0,48905
Rpl10	2,930E6	4,042E6	6,781E5	0,000E0	2,163E6	4,130E6	5,536E6	0,000E0	5,903E6	1,559E7	7,711E6	6,289E6	0,45862
Hspa8	1,428E7	2,550E7	2,224E7	1,470E7	8,789E6	1,438E7	3,591E7	0,000E0	6,525E7	3,986E7	4,905E7	4,410E7	0,43835
Myo1c	7,267E6	8,078E6	9,209E6	6,046E6	4,695E6	1,051E7	1,043E7	0,000E0	1,303E7	1,425E7	1,890E7	1,821E7	0,42158
Pkm	4,386E7	5,690E7	4,582E7	3,158E7	4,644E7	5,207E7	4,168E7	0,000E0	1,042E8	6,132E7	1,099E8	9,937E7	0,41980
Hnrnpa3	0,000E0	6,370E6	4,076E6	3,090E6	2,454E6	5,300E6	6,635E6	0,000E0	3,698E6	9,019E6	8,620E6	8,657E6	0,39352
Ehd4	2,676E6	1,130E6	1,913E6	2,136E6	5,433E5	2,672E6	2,786E6	0,000E0	0,000E0	2,845E6	3,037E6	5,306E6	0,38174

Selection criteria:
1. Both of the duplicates in Amot p130 + Biotin group has positive values.
2. Either of the duplicates in Amot p130 + Biotin group is less than any of the control groups (Ctrl -/+ Biotin, p80/p130 -Biotin).

Color code	1,000E0	2,000E0	3,000E0	4,000E0	5,000E0	6,000E0	7,000E0	8,000E0	9,000E0	1,000E1	1,100E1	1,200E1

Table S4. Panther pathway analysis of p130-Amot BioID pulldown. Related to Figure 5

Term	Overlap	P-value	Adjusted P-value	Log10 adjusted P-vaue	Genes
Integrin signalling pathway Homo sapiens P00034	9/156	1,16E-05	6,51E-04	3,186273143	ACTN1;CAV1;FLNA;FLNB;ACTN4;TLN1;CRK;RHOA;CRKL
Parkinson disease Homo sapiens P00049	7/81	8,14E-06	9,12E-04	3,040062684	YWHAE;HSPA9;PSMA6;HSPA8;YWHAQ;PSMA1;YWHAB
Pentose phosphate pathway Homo sapiens P02762	2/8	0,002152737	0,060276622	1,219851091	TALDO1;PGD
Pyruvate metabolism Homo sapiens P02772	2/8	0,002152737	0,08036883	1,094912354	PKM;PC
Huntington disease Homo sapiens P00029	5/124	0,005190295	0,116262598	0,934559975	VAT1;ACTR2;DYNC1H1;CAPN2;DYNLL1
DNA replication Homo sapiens P00017	2/19	0,01232486	0,230064059	0,638151223	TOP2A;TOP1
Nicotine pharmacodynamics pathway Homo sapiens P06587	2/28	0,025852072	0,361929006	0,44137661	FLNA;KCNK3
Cytoskeletal regulation by Rho GTPase Homo sapiens P00016	3/70	0,024916444	0,398663097	0,399393963	CFL1;MYH9;MYH10
Angiogenesis Homo sapiens P00005	4/142	0,03891336	0,484255152	0,31492575	DVL2;CRK;RHOA;CRKL
Asparagine and aspartate biosynthesis Homo sapiens P02730	1/5	0,043960207	0,492354318	0,307722249	ASNS
Serine glycine biosynthesis Homo sapiens P02776	1/6	0,052518882	0,534737705	0,271859193	PSAT1
FGF signaling pathway Homo sapiens P00021	3/99	0,059318151	0,553636072	0,256775621	YWHAE;YWHAQ;YWHAB
Dopamine receptor mediated signaling pathway Homo sapiens P05912	2/52	0,078984415	0,631875319	0,199368608	FLNA;KCNK3
EGF receptor signaling pathway Homo sapiens P00018	3/109	0,074525034	0,642061832	0,192423147	YWHAE;YWHAQ;YWHAB
Inflammation mediated by chemokine and cytokine signaling pathway Homo sapiens P00031	4/188	0,088804017	0,663069991	0,178440627	CAMK2D;MYH9;MYH10;RHOA
Opioid proopiomelanocortin pathway Homo sapiens P05917	1/18	0,149468589	0,727847044	0,137959878	KCNK3
Glycolysis Homo sapiens P00024	1/17	0,141781006	0,756165367	0,121383218	PKM
Opioid proenkephalin pathway Homo sapiens P05915	1/18	0,149468589	0,760931	0,118654722	KCNK3
5HT4 type receptor mediated signaling pathway Homo sapiens P04376	1/16	0,13402433	0,790038158	0,102351932	KCNK3
Axon guidance mediated by semaphorins Homo sapiens P00007	1/17	0,141781006	0,793973635	0,100193919	RHOA

178 proteins (fc>0) listed in Table S3
Top 20 enrtiched pathways
Statistical information
http://amp.pharm.mssm.edu/Enrichr

Table S5. Primers for genotyping. Related to Key Resources Table.

Primers	Sequences	Conpany
Amot flox/flox	5’-GATGGATGCTATGAGAAGGTG-3’ 5’-GTAAGGATTACAGAGTCTGGG -3’	Thermo Fisher Scientific
Amot KO	5’-ATAGCTAGTGAGCAGTAGCAG-3’ 5’-GTAAGGATTACAGAGTCTGGG -3’	Thermo Fisher Scientific
CDH5-Cre	5’-GCCTGCATTACCGGTCGATGCAACGA-3’ 5’-GTGGCAGATGGCGCGGCAACACCATT-3’	Thermo Fisher Scientific
YFP reporter	5’-AAA GTC GCT CTG AGT TGT TAT-3’ 5’-GGA GCG GGA GAA ATG GAT ATG-3’ 5’-GCG AAG AGT TTG TCC TCA ACC-3’	Thermo Fisher Scientific